

A Numerical Methodology for Efficient Evaluation of 2D Sommerfeld Integrals in the Dielectric Half-Space Problem

Amit Hochman, *Member, IEEE*, and Yehuda Leviatan, *Fellow, IEEE*

Abstract—The analysis of 2D scattering in the presence of a dielectric half-space by integral-equation formulations involves repeated evaluation of Sommerfeld integrals. Deformation of the contour to the steepest-descent path results in a well-behaved integrand, that can be readily integrated. A well-known drawback of this method is that an analytical expression for the path is available only for evaluation of the reflected fields, but not for the evaluation of the transmitted fields. A simple scheme for numerical determination of the steepest-descent path, valid for both cases, is presented. The computational cost of the numerical determination is comparable to that of evaluating the analytical expression for the steepest-descent path for reflected fields. When necessary, contributions from branch-cut integrals and a second saddle point are taken into account. Certain ranges of the input parameters, which result in integrands that vary rapidly in the neighborhood of the saddle point, require special treatment. Alternative paths and specialized Gaussian quadrature rules for these cases are also proposed. An implementation of the proposed numerically determined steepest-descent path (ND-SDP) method is freely available for download.

Index Terms—Green functions, integral equations, method of moments (MoM), nonhomogeneous media, Sommerfeld integrals.

I. INTRODUCTION

THE determination of the fields of an elementary source radiating in plane-stratified media is a canonical problem in electromagnetics. Even though some variants of this problem have been the subject of research since the beginning of the 20th century [1], [2], they are still of interest today. Comprehensive references are [3]–[5], and reviews of computational aspects can be found in [6]–[8]. Nowadays, interest is largely motivated by integral-equation formulations for scattering and propagation problems, as they entail repeated evaluation of the fields of elementary sources that constitute the Green's function. The starting point for the evaluation of the various Green's functions is an integral representation of the fields (or potentials), of the Sommerfeld integral (SI) type. Although the literature on SI evaluation is vast and the procedures are varied, most methods include some or all of the following steps.

Manuscript received November 05, 2008; revised May 14, 2009. First published December 04, 2009; current version published February 03, 2010. This research was supported in part by the Israel Science Foundation.

The authors are with the Department of Electrical Engineering, Technion-Israel Institute of Technology, Haifa 32000, Israel (e-mail: amith@tx.technion.ac.il; leviatan@ee.technion.ac.il).

Color versions of one or more of the figures in this paper are available online at <http://ieeexplore.ieee.org>.

Digital Object Identifier 10.1109/TAP.2009.2037761

- *Contour Deformation*: The integration contour is deformed from the real axis to a contour on the complex plane. The purpose of this step is to obtain a more well-behaved integrand by avoiding pole and branch-point singularities and possibly also minimizing phase variation along the path. Some possible paths are given in [9]–[11].
- *Singularity Subtraction*: Singular terms of the integrand are subtracted and then added back after analytical integration. This step has been used together with contour deformation [12], [13], or as an alternative to it [14].
- *Numerical Integration*: The value of the integral is estimated from a finite number of samples of the integrand. When this is done by a quadrature rule, the estimate is a linear combination of the samples of the integrand. In a more sophisticated scheme, the integrand (or some part of it) is approximated by a superposition of complex exponentials and this approximation is then integrated analytically [15]. This so-called Discrete Complex Image Method (DCIM), which has found widespread use [16], [17], is closely related to the continuous complex image method [18]. In a similar technique [19], the integrand is approximated by a superposition of rational functions, and the resulting approximation is then integrated analytically.

Among the possible integration contours, the steepest-descent path (SDP) passing through a saddle point is considered, in some respects, the optimal choice [20].

Another aspect of using the SDP is that if, in the process of deforming the original path to the SDP, a branch point is intercepted, a path surrounding the intercepted branch point must be added. Although this entails some book-keeping, it also highlights an appealing feature of the method, namely, that the integral is obtained as a sum of distinct, physically meaningful, contributions. From a computational point of view, as simple quadrature is used, this method can potentially outperform the popular DCIM which involves finding the complex images by more computationally intensive methods such as Prony's method [12], or the matrix pencil method [21]. Moreover, evaluating the Green's function along the SDP is essential for the fast inhomogeneous plane wave algorithm [22] which can be used to solve electromagnetically large layered-media problems in $O(N \log N)$ computational complexity.

When the observation point and the source point are in the same medium, an analytical expression for the SDP is available, and it has been used extensively [6], [23], [24]. In contrast, when the source and observation points are not in the same medium, an analytical expression for the SDP is not available. One op-

tion, in this latter case, is to determine the path numerically, but this was deemed too computationally expensive, or otherwise impractical [23], [25].

In this paper, a simple and efficient scheme for numerical determination of the SDP is presented. Using this scheme, path determination is not slower than evaluating the analytical expression for the SDP, available for the reflected fields. The numerically-determined SDP (ND-SDP) can thus complement earlier works which used only the analytically known SDP. An example of such a work is that of Cui and Chew [23] in which the electric line-source case was studied. In [23], the analytically obtained SDP was used for the reflected fields, whereas for the transmitted fields, it was assumed that the observation point was close enough to the interface so that an analytically determined approximation of the SDP could be used. In the present work, the SDP is determined numerically both for the reflected and transmitted fields of electric and magnetic line-sources. As far as the determination of the SDP is concerned, the reflected and transmitted fields can be treated equally, by use of the same code. The handling of intercepted branch points, however, should be different. For example, when a branch point is intercepted in the transmitted field case, a contribution from a second saddle point must be taken into account.

Following earlier works that used the SDP [6], [23], the numerical integration employed throughout is Gaussian quadrature. An attractive feature of Gaussian quadrature is that it has only one parameter that must be set by the user, namely, the number of integration points. The integration points and the weights are then determined by the rule. We preserve this feature by deriving all the values of the parameters in the numerical scheme from the number of integration points.

For certain combinations of source and observation point coordinates and material parameters, the integrand varies rapidly on the SDP and it becomes difficult to integrate it efficiently. This problem is well-known (see for example the introduction of [8]), and it is not particular to numerically determined SDPs. The parameters for which these difficulties are encountered correspond to three different physical cases, as follows.

- *Critical angle case*: Occurs in the calculation of the reflected fields, when the source is in the dense medium, and the angle of specular reflection is close to the critical angle. This case was considered in [23], where the authors resorted to a uniform asymptotic expansion.
- *Grazing angle case*: Occurs when the source and observation points are both near the interface, but far apart laterally, on a wavelength scale.
- *Quasi-static case*: Occurs when the source and observation points are both near the interface, and close to each other laterally, on a wavelength scale. The difficulties encountered in this case were discussed in [26].

In all three cases the problem is mathematically similar and can be explained as follows. When evaluated on the SDP, the exponential factor of the integrand resembles a Gaussian curve, and its standard deviation can be used to define a neighborhood of the saddle point from which the dominant contribution to the integral comes. If the other factors, such as the amplitude and the reflection or transmission coefficients, vary rapidly in this neighborhood, the integration becomes difficult. As the most

rapid variation of these other factors is near the branch points, the difficulties arise when the saddle point is close to one of the branch points, *on a standard-deviation scale*. This can happen in two different ways. One is when the saddle point approaches the branch point, which occurs when the angle of specular reflection approaches the critical angle or becomes a grazing angle. The other, which occurs in the quasi-static case, is when the standard deviation increases to the extent that a branch point is included in the neighborhood of the saddle point. Assuming the number of Gaussian integration points is kept constant, the accuracy will deteriorate in these cases.

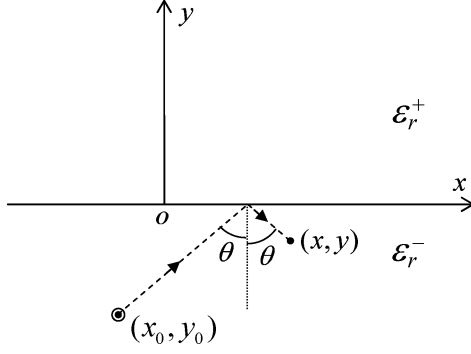
Although each of the three cases is handled differently, all solutions are based on integration along an alternative path by use of a Gaussian quadrature rule that is tailored to the behavior of the integrand on the path. In the critical- and grazing-angle cases, the Gaussian quadrature rules used are the generalized Hermite and Laguerre rules, which are known from the classical theory of orthogonal polynomials [27]. The Gaussian quadrature rules used in the quasi-static case, on the other hand, are derived by so-called *discretization methods*, which can generate these rules for quite arbitrary weight functions [28]. Appropriate weight functions are determined according to the behavior of the integrand on an alternative path, and their corresponding quadrature rules are derived. The rules are specific to the field component being calculated and to the material parameters. Once the rules are derived (a process which takes on the order of a second) they can be applied to all relevant source and observation point pairs.

The techniques described in this paper have been combined in a MATLAB computer program that yields accurate results for a wide range of input parameters in very short execution time. One of the advantages of the ND-SDP method is that it can be easily vectorized. This means that all operations can be done by functions that operate on vectors of the input parameters, yielding a considerable reduction in function-call overhead. The program, which operates in this vectorized fashion, is freely available for download [29].

The remainder of this paper is organized as follows. The various integrals that are to be solved are summarily formulated in Section II. Next, the numerical determination of the SDP is explained in Section III, and the inclusion of contributions from intercepted branch points is discussed in Section IV. The cases for which integration along the SDP yields poor results: the critical-angle case, the grazing-angle case, and the quasi-static case are considered in Sections V–VII. Numerical results are shown in Section VIII, and the paper is summarized in Section IX.

II. PROBLEM STATEMENT AND FORMULATION

The configuration to be considered is that of a unit-amplitude electric line-source (ELS) or a magnetic one (MLS) situated in one of two contiguous dielectric half-spaces, as shown in Fig. 1. The coordinates of the line-source are (x_0, y_0) and it is oriented in the z direction, i.e., parallel to the interface. It is assumed throughout that $y_0 < 0$, as the $y_0 > 0$ case can be treated by symmetry considerations. The relative permittivities of the $y < 0$ and $y > 0$ regions are denoted by ϵ_r^- and ϵ_r^+ , respectively, and for both regions the permeability is taken to be that of free-space, μ_0 . The free-space permittivity is denoted

Fig. 1. Two contiguous dielectric half-spaces, with a line-source at (x_0, y_0) .

by ε_0 . All fields and sources are assumed to follow a harmonic $\exp(j\omega t)$ time dependence, which is suppressed.

The fields in this configuration are well-known, and they can be expressed as follows:

$$\mathbf{E}_{\text{tot}} = \begin{cases} \mathbf{E}^t & \text{for } y \geq 0 \\ \mathbf{E}^i + \mathbf{E}^r & \text{for } y < 0 \end{cases} \quad (1a)$$

$$\mathbf{H}_{\text{tot}} = \begin{cases} \mathbf{H}^t & \text{for } y \geq 0 \\ \mathbf{H}^i + \mathbf{H}^r & \text{for } y < 0 \end{cases} \quad (1b)$$

where \mathbf{E}^i and \mathbf{H}^i are the fields of the line-source in a homogeneous material of relative permittivity ε_r^- . They do not require an integral representation and can be evaluated in closed form (see, for example, [30, p. 224]). The reflected fields, \mathbf{E}^r and \mathbf{H}^r , can be expressed in terms of integrals of the following form:

$$I_r = \frac{1}{4\pi} \int_{\mathcal{P}} A_r(k_x) R(k_x) e^{-j\alpha_r(k_x)} dk_x \quad (3)$$

where the complex phase function $\alpha_r(k_x)$ is given by

$$\alpha_r(k_x) = k_x |x - x_0| - k_y^-(y + y_0) \quad (4)$$

and k_y^- is related to k_x through the separation equation in the $y < 0$ region, i.e.,

$$(k^-)^2 = (k_y^-)^2 + k_x^2 \quad (5)$$

in which $k^- = (\omega/c)\sqrt{\varepsilon_r^-}$ is the wave number in the $y < 0$ region, with c being the speed of light in free-space. In (3), the reflection coefficient $R(k_x)$ is given by

$$R(k_x) = \begin{cases} \frac{k_y^- - k_y^+}{k_y^- + k_y^+} & \text{for ELS} \\ \frac{k_y^- \varepsilon_r^+ - k_y^+ \varepsilon_r^-}{k_y^- \varepsilon_r^+ + k_y^+ \varepsilon_r^-} & \text{for MLS} \end{cases} \quad (6a)$$

$$(6b)$$

where k_y^- is related to k_x via (5), and k_y^+ is related to k_x through the separation equation in the $y > 0$ region, i.e.,

$$(k^+)^2 = (k_y^+)^2 + k_x^2 \quad (7)$$

TABLE I
EXPRESSIONS FOR I_r AND $A_r(k_x)$ IN (3)

I_r		$A_r(k_x)$
ELS	MLS	
$-\mu_0\omega E_z$	$-\varepsilon_0\varepsilon_r^-\omega H_z$	$1/k_y^-$
H_x	E_x	1
$\text{sgn}(x-x_0)H_y$	$\text{sgn}(x-x_0)E_y$	k_x/k_y^-

TABLE II
EXPRESSIONS FOR I_t AND $A_t(k_x)$ (8)

I_t		$A_t(k_x)$
ELS	MLS	
$-\mu_0\omega E_z$	$-\varepsilon_0\varepsilon_r^-\omega H_z$	$1/k_y^-$
$-H_x$	$(\varepsilon_r^-/\varepsilon_r^+)E_x$	k_y^+/k_y^-
$\text{sgn}(x-x_0)H_y$	$-(\varepsilon_r^-/\varepsilon_r^+)\text{sgn}(x-x_0)E_y$	k_x/k_y^-

in which $k^+ = (\omega/c)\sqrt{\varepsilon_r^+}$ is the wave number in the $y > 0$ region. For future reference, we will use k^{dn} to denote $\max(k^-, k^+)$, and k^{th} to denote $\min(k^-, k^+)$. The integration path \mathcal{P} in (3) stays on the real axis except near the branch points at $k_x = k^\pm$ where it is indented into the first and third quadrants. The correspondence between the integral I_r and the various reflected field components is shown, together with the appropriate amplitude functions $A_r(k_x)$, in Table I.

Like the reflected fields, the transmitted fields, \mathbf{E}^t and \mathbf{H}^t , can be expressed in terms of similar integrals. We have

$$I_t = \frac{1}{4\pi} \int_{\mathcal{P}} A_t(k_x) T(k_x) e^{-j\alpha_t(k_x)} dk_x \quad (8)$$

where the complex phase function $\alpha_t(k_x)$ is given by

$$\alpha_t(k_x) = k_x |x - x_0| + k_y^+ y - k_y^- y_0 \quad (9)$$

and the transmission coefficient $T(k_x)$ is given by

$$T(k_x) = \begin{cases} \frac{2k_y^-}{k_y^- + k_y^+} & \text{for ELS} \\ \frac{2k_y^- \varepsilon_r^+}{k_y^- \varepsilon_r^+ + k_y^+ \varepsilon_r^-} & \text{for MLS} \end{cases} \quad (10a)$$

$$(10b)$$

In Table II, the correspondence between the integral I_t and the various transmitted field components is shown, together with the appropriate amplitude functions $A_t(k_x)$. Field components not shown in Tables I–II are zero.

To unify a number of formulas in the sequel, pertaining to the reflected and transmitted fields, it is convenient to introduce a “unified” complex phase function, α_u , which is equal to α_r for the reflected fields, and to α_t for the transmitted fields. This function can be written succinctly as

$$\alpha_u = |x - x_0| k_x + y^- k_y^- + y^+ k_y^+ \quad (11)$$

where y^- and y^+ are given by

$$y^- = |y_0| + |y|, \quad y^+ = 0 \quad (12)$$

for the reflected fields, and by

$$y^- = |y_0|, \quad y^+ = y. \quad (13)$$

for the transmitted fields. Lastly, to ensure proper behavior at infinity, we require

$$\text{Im}(k_y^-) \leq 0, \quad \text{Im}(k_y^+) \leq 0. \quad (14)$$

The integrals in (3) and (8) have no known analytical expression and they are notoriously difficult to evaluate numerically. This is because the integrands are rapidly oscillating and slowly decaying. As already mentioned, the approach proposed in this paper consists of deforming the integration contour from the original path P to the SDP. As we assume that the half-spaces are lossless and of positive permittivity, no poles are intercepted in the course of the deformation. However, branch points of the integrand at $k_x = \pm k^-$ and $k_x = \pm k^+$ may be intercepted. In this case, a path surrounding the intercepted branch point must be added. It should be remarked that in the integrand of I_r , the branch points at $k_x = \pm k^+$ appear only in the reflection coefficient but not in the complex phase function α_r . On the other hand, in the integrand of I_t , the two branch points appear both in the transmission coefficient and in the complex phase function α_t . It is due to this essential difference that the calculation and analysis of the transmitted fields is in general more complicated.

III. NUMERICALLY DETERMINED STEEPEST-DESCENT PATHS

With the aid of the Cauchy-Riemann equations, the SDP can be shown to coincide with the level curve of the function $\text{Re}[\alpha_u(k_x)]$ that passes through the saddle point. Denoting the k_x value of the saddle point by k_{sp} , this curve is given implicitly by

$$\text{Re}[\alpha_u(k_x)] = \text{Re}[\alpha_u(k_{\text{sp}})]. \quad (15)$$

For the reflected field, it is possible to manipulate (15) to obtain an explicit expression for $k_x''(k_x')$, the imaginary part of k_x , in terms of its real part. This, however, is not possible for the transmitted field, because the form of $\alpha_t(k_x)$ is more complicated. In this case, determining $k_x''(k_x')$ entails the solution of a non-linear equation for each point of the curve. The observation that allows fast determination of the SDP is that even when there is no analytical solution to (15), there is always an analytical expression for the direction of steepest descent at any point in the complex k_x plane. This can be used to approximate the SDP by a piecewise-linear path, obtained by stepping in the direction of steepest descent with a constant step size δ , beginning at the saddle point [see Fig. 2(a)]. This process continues until the

traced path is as long as required by the Gaussian quadrature rule that is used to evaluate the integral, once the path is determined. To facilitate efficient integration, the piecewise-linear path is then approximated by a low-order polynomial that is fitted to the path vertices, in a least-squares sense. In this way we obtain a parametric representation of an approximate SDP that can be written in terms of a real parametric variable τ , as $k_x(\tau) = k_x'(\tau) + jk_x''(\tau)$. We then have,

$$\int_{\text{SDP}} f(k_x) dk_x = \int_{-\infty}^{\infty} f[k_x(\tau)] \left[\frac{dk_x(\tau)}{d\tau} \right] d\tau \quad (16)$$

where $f(k_x)$ is any of the integrands of (3) or (8). To this transformed integrand, Gaussian quadrature, which requires a real integration variable, can be readily applied. Clearly, the parametric representation should be smooth, otherwise the multiplication by its derivative will destroy the smoothness of the transformed integrand. This is why a low-order polynomial representation is preferred over a piecewise-linear one. Once the polynomial is found, the integration points are distributed in the range of τ according to the Gaussian quadrature rule, and the derivative of the path at these points, also required for the integration, is evaluated. An illustration of this scheme is depicted in Fig. 2(b).

The parameters of the path determination scheme are set as follows. First, the number of integration points, denoted m , is set by the user, according to the desired trade-off between accuracy and computation time. This trade-off is investigated in some detail in Section VIII. We take the number of vertices of the piecewise-linear path equal to m . The step size δ is taken to be equal to the average Gaussian spacing between integration points. This ensures that the length of the piecewise-linear path fits the Gaussian quadrature rule. Also, since the step size of the Gaussian quadrature rule is scaled to fit the variation of the integrand, this choice usually provides an adequate step size for the calculation of the path. Lastly, we take a small number for the order of the polynomial: we have experimented with orders in the range of 5–25, and as long as the order is sufficiently smaller than m (less than $\approx m/2$) the exact value does not seem to matter much.

Although this procedure may appear to involve significant overhead, we show below how it can be expedited if m is kept constant for many pairs of source and observation points. Keeping m constant also allows all operations to be vectorized, thus reducing function-call overhead considerably. Clearly, to be practical the method must therefore yield accurate results for a broad range of parameters, using a constant number of integration points. On the other hand, it is assumed that operations that are done once for a given m (regardless of the number of pairs of source and observation points) may take longer without affecting the overall efficiency.

A. Saddle Points

The starting points for the SDP computation are the saddle points that are obtained from the condition that the derivative of the complex phase function vanish at the saddle point. When

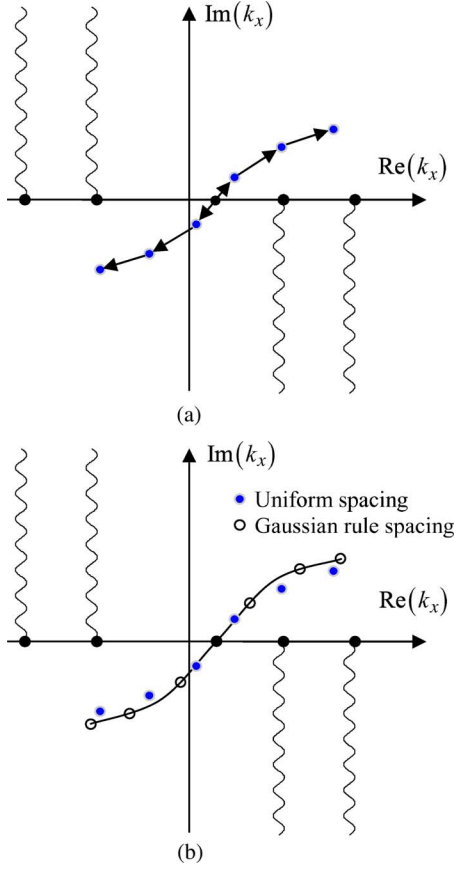


Fig. 2. Illustration of the numerical scheme for the determination of the SDP. In (a), the m uniformly distributed points are obtained by tracing the SDP, starting at the saddle point. In (b), a low-order polynomial is fit to the uniformly spaced points. Then, the integration points are distributed on the path defined by the polynomial according to the Gaussian quadrature rule.

calculating the reflected fields, the saddle point is determined readily as

$$k_{\text{sp}} = \frac{k^- |x - x_0|}{\sqrt{(x - x_0)^2 + (y + y_0)^2}} = k^- \sin \theta \quad (17)$$

where θ is the angle shown in Fig. 1 between the normal to the interface and the ray that reaches the observation point by specular reflection. When calculating the transmitted fields, the determination of the saddle point leads to a quartic equation in k_{sp}^2 . The four solutions of the quartic equation lead to eight candidate solutions for k_{sp} , not all of which are zeros of the derivative of the complex phase function on the relevant Riemann-sheet. As discussed in [31], two such solutions are relevant. In the lossless case, there is one solution on the portion of the real axis between the origin and the branch point of the thin medium, and one complex solution. To determine which of the eight candidate solutions are the two relevant ones, we evaluate the derivative on the relevant Riemann-sheet for all candidate solutions. The absolute value of the derivative is then a measure of the error of the solution, and it is seldom exactly zero for any of the candidate solutions. We take as the relevant solutions the real solution with smallest error, and the complex solution with smallest error.

B. Numerical Determination of the SDP

In the first stage of the algorithm, points on an approximate SDP are determined by stepping in the direction of steepest descent, beginning at the saddle point. Let \vec{s} denote a column vector of the m complex k_x values along the yet to be determined SDP, where, for convenience, m is assumed even. At the saddle-point, the angle between the SDP and the real-axis is $\pi/4$ [4, Ch. 4.1b]. Hence, the i th element of \vec{s} , s_i , is calculated by first setting the two middle elements, $s_{m/2}$ and $s_{m/2+1}$, to $k_{\text{sp}} - \exp(j\pi/4)\delta/2$ and $k_{\text{sp}} + \exp(j\pi/4)\delta/2$, respectively. The rest of the s_i are then calculated by the iterative formulas

$$s_{i+1} = s_i + \delta \hat{w}_i, \text{ for } i = \frac{m}{2} + 1, \frac{m}{2} + 2, \dots, m-1 \quad (18)$$

$$s_{i-1} = s_i + \delta \hat{w}_i, \text{ for } i = \frac{m}{2}, \frac{m}{2} - 1, \dots, 2 \quad (19)$$

where \hat{w}_i is a unit-amplitude complex number, given by

$$\hat{w}_i = \frac{(-jw_i)^*}{|w_i|} \quad (20)$$

which, when interpreted as a unit vector in the complex k_x plane, points in the direction of steepest descent. Here, w_i denotes the derivative of the unified complex phase function, α_u , evaluated at the point $k_x = s_i$. Explicitly, w_i is given by

$$w_i = |x - x_0| - \frac{y^+ s_i}{\sqrt{(k^+)^2 - s_i^2}} - \frac{y^- s_i}{\sqrt{(k^-)^2 - s_i^2}}. \quad (21)$$

In (21), the signs of the radicals will differ from the proper choice in (14) whenever the path crosses a branch cut into an improper Riemann-sheet.

When calculating the reflected fields, the computational cost of the numerical determination of the SDP can be compared with the computational cost of evaluating the analytical formula for the SDP in the reflected field case

$$s_i'' = \frac{[(k^-)^2 - s_i' k_{\text{sp}}] (s_i' - k_{\text{sp}})}{\sqrt{(k^- - k_{\text{sp}})^2 [(k^-)^2 + (s_i')^2 - 2s_i' k_{\text{sp}}]}} \quad (22)$$

where $s_i = s_i' + js_i''$. Clearly, the cost of evaluating s_i is roughly the same either way. It must be noted, however, that (22) gives the exact SDP, whereas (18), (19) only yield an approximation to it. Nevertheless, the error of the approximation, which is $O(\delta^2)$ for each step, does not alter the general behavior of the integrand on the path appreciably.

After the m points on the approximate SDP path are determined, an analytical parametric representation of the path is obtained and the points are distributed according to a Gaussian quadrature rule (to be specified in Section III-D).

C. Parametric Representation of the Path

An analytical parametric representation of the numerically determined path is obtained by fitting a low-order complex poly-

nomial, $p(\tau)$, to the points s_i , calculated by (18), (19). For an n th order polynomial $p(\tau)$, given by

$$p(\tau) = p_{n+1}\tau^n + p_n\tau^{n-1} + \dots + p_1 \quad (23)$$

we denote by \vec{p} an $(n+1)$ -element column vector of its (yet to be determined) complex coefficients. The m values of τ which correspond to the points s_i are set, arbitrarily, to $\tau_i = -1 + 2(i-1)/(m-1)$, i.e., they are uniformly distributed in the $[-1, 1]$ interval. The p_i are then obtained by solving the following linear system in a least-squares error sense:

$$[V]\vec{p} = \vec{s} \quad (24)$$

where $[V]$ denotes the $m(n+1)$ Vandermonde matrix whose ij th element is τ_i^{j-1} . As is well-known, this solution of (24) is given by

$$\vec{p} = [V]^+ \vec{s} \quad (25)$$

where $[V]^+$ denotes the pseudo-inverse of $[V]$, which can be obtained from a singular-value decomposition of $[V]$. When the Green's function has to be evaluated many times for different pairs of source and observation points, the various path vectors \vec{s} can be arranged in a matrix $[S]$, and the corresponding vectors of polynomial coefficients can be arranged in a matrix $[P]$. Since $[V]$ and $[V]^+$ depend only on m , the matrix $[P]$ is given by

$$[P] = [V]^+ [S] \quad (26)$$

where it is assumed that m is kept constant for all paths. In this way, the matrices $[V]$ and $[V]^+$ are computed only once, regardless of the number of source and observation point pairs. Other than the short time required to calculate $[V]^+$ once, the calculation of each coefficient of a polynomial requires just m complex multiplications, and the calculation of all the coefficients of a polynomial requires $m(n+1)$ complex multiplications. In fact, since only $[S]$ is complex, whereas $[V]$ is real, the number of (real) multiplications is $2m(n+1)$.

Once the polynomials have been obtained, they must be evaluated in order to redistribute the points along the path. The new points, $[\tilde{S}]$, are given by $[\tilde{S}] = [\tilde{V}][P]$, where $[\tilde{V}]$ denotes the Vandermonde matrix that corresponds to the points distributed according to the Gaussian quadrature rule. The ij th element of this matrix is given by $\tilde{\tau}_i^{j-1}$, with $\tilde{\tau}_i$ the Gaussian quadrature rule points scaled to fit the $[-1, 1]$ interval. Similarly, the derivatives of the paths at the $[\tilde{S}]$ points, $[S_d]$, are given by $[S_d] = [\tilde{V}_d][P_d]$, where $[P_d]$ holds the coefficients of the differentiated polynomials, and $[\tilde{V}_d]$ is the corresponding Vandermonde matrix which is obtained from $[\tilde{V}]$ by omitting its last (highest-power) column. Similarly to the $[V]$ matrix, the $[\tilde{V}]$ and $[\tilde{V}_d]$ matrices are computed only once, regardless of the number of source and observation-point pairs. Other than the short time required to calculate these matrices once and for all, the calculation of each path requires $2m(n+1)$ additional multiplications,

TABLE III
ANALYTICAL VS. NUMERICAL DETERMINATION OF THE SDP

	Analytical formula	Numerical determination
Determine path	m evaluations of (22) $\approx 95m$ multiplications	m gradient evaluations
Determine polynomial and distribute points along it	N/A	$4(n+1)m$ multiplications
Evaluate path derivative	m gradient evaluations	$2nm$ multiplications
Overall cost	m gradient evaluations + $\approx 95m$ multiplications	m gradient evaluations + $(6n+4)m$ multiplications

and the evaluation of the derivatives requires $2mn$ multiplications.

It is worth mentioning that when an analytical formula for the SDP is used, the derivative of the path must still be calculated by (20), (21), with the s_i of the exact path. The computational cost of this calculation equals the computational cost of the calculation used to trace out the path numerically. It turns out then, that to compare the times of analytical vs. numerical determination of the SDP, one should compare the time it takes to calculate $[\tilde{S}]$ and $[S_d]$ given $[S]$, with the time it takes to evaluate (22). The computational complexity of both calculations is $O(m)$, assuming n to be a small constant. Typically, $n < 10$, and the calculation of $[\tilde{S}]$ and $[S_d]$ given $[S]$ requires $6n+4$ multiplications per point. Since (22) includes a rather costly square-root operation, equivalent to about 85 multiplications in our system, its evaluation is not faster than the numerical determination. This comparison is summarized in Table III.

D. Gaussian Quadrature Rule for Approximating the SDP Integral

Bearing in mind that along the SDP the integrand has a Gaussian envelope, the most natural quadrature rule to apply is the Hermite-Gaussian rule. An m -point quadrature rule of this type is known to yield an exact result for integrands that are polynomials of degree $2m-1$ multiplied by a Gaussian weight function [32]. In this work, however, two half-range Hermite-Gaussian rules [28, p. 88], each with $m/2$ points were used for each half of the SDP. The lower order of each half adds robustness, which is particularly useful when the saddle point approaches a branch point. As the width of the Gaussian changes from one observation point to the next, the integration points and weights must be scaled according to the standard deviation of the Gaussian. The required standard deviation, σ , is readily determined from the second derivative of the complex phase function α_u at the saddle point. We have

$$\sigma = \frac{1}{\sqrt{\left| \frac{\partial^2 \alpha_u}{\partial k_x^2} \right|_{k_x=k_{sp}}}}. \quad (27)$$

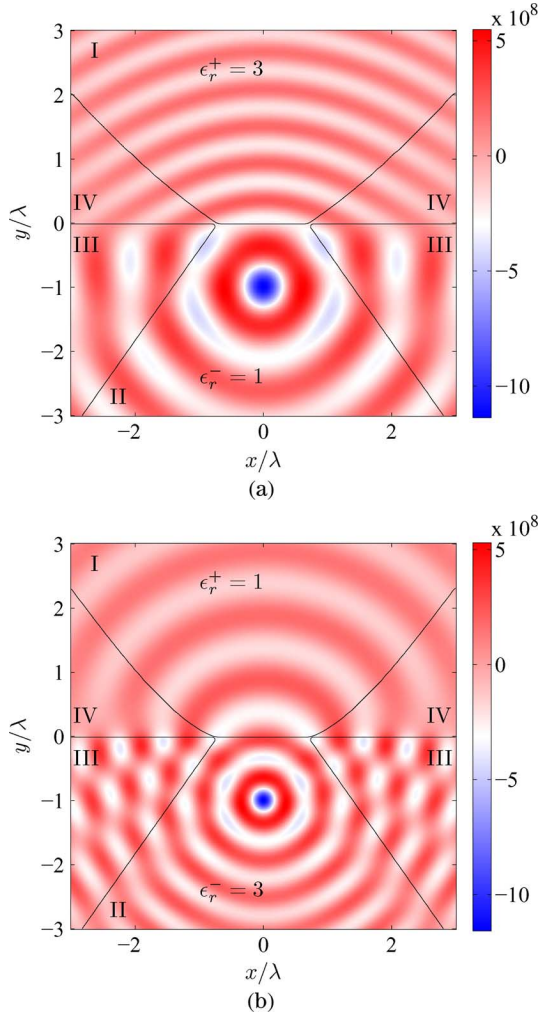


Fig. 3. The real part of the z component of the electric field due to a unit amplitude ELS. In regions I and II no branch points are intercepted. In (a), the source is in the optically thin medium. In (b), the source is in the optically dense medium. In region III, the branch point associated with the $y > 0$ region is intercepted, and in region IV the complex saddle point is intercepted.

IV. INTERCEPTED BRANCH POINTS

In the course of deforming the original path to the SDP, the branch points may be intercepted. If this happens, an integral around the intercepted branch point must be added to the SDP contribution.

A. Reflected Fields

When calculating the reflected fields, an intercepted branch point leads to the well-known lateral wave contribution [4, p. 508]. In the lossless case assumed here, the branch point is intercepted whenever

$$\sin \theta > \sqrt{\frac{\epsilon_r^{\text{th}}}{\epsilon_r^{\text{dn}}}} \quad (28)$$

where ϵ_r^{th} and ϵ_r^{dn} are the relative permittivities of the optically thin and the optically dense media, respectively. It follows that the branch point is intercepted whenever the angle of the specular reflection θ is beyond an angle $\theta_c = \sin^{-1}(\sqrt{\epsilon_r^{\text{th}}/\epsilon_r^{\text{dn}}})$,

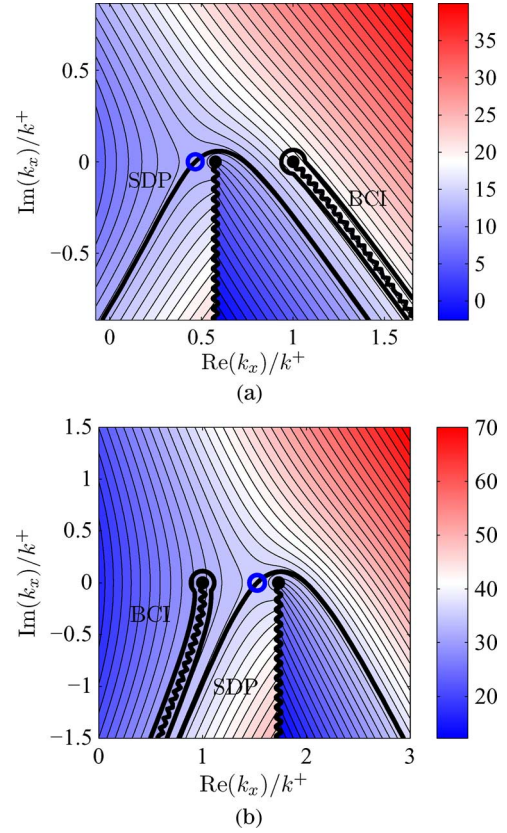


Fig. 4. The real part of the complex phase function of the reflected fields, α_r , overlaid with contours of constant $\text{Re}(\alpha_r)$. The thick line shows the path used by the algorithm, and the circle marker marks the saddle point. The branch point of the $y > 0$ region is intercepted, necessitating the addition of a BCI. In (a), the source is in the optically thin medium. In (b), the source is in the optically dense medium.

which, in the case of a wave propagating in a dense medium and impinging on an interface with a thin medium, is the well-known critical angle. Note that although this critical angle does not have the total internal reflection physical interpretation when the source is in the thin medium, condition (28) applies regardless of whether the source is in the dense medium or the thin medium. In the latter case, the lateral wave contribution is evanescent [3, p. 263].

The region in physical space which corresponds to the branch point being intercepted is shown in Fig. 3, where it is marked as region III. The lines delimiting the regions have been plotted on top of an image of the z component of the electric field due to a unit amplitude ELS, as calculated by use of the ND-SDP method. The case of the source being in the thin medium is shown in physical space in Fig. 3(a), and in the complex k_x plane in Fig. 4(a). The complementary case, when the source is in the dense medium is shown in physical space in Fig. 3(b), and in the complex k_x plane in Fig. 4(b).

The branch-cut integral (BCI) that must be added to the SDP contribution is calculated along paths shown in Fig. 4. The BCI path surrounds the branch cut, which is taken along the steepest-descent path that originates at the branch point. In practice, the two halves of the path are taken infinitesimally close to the branch cut. This path has been used in [20], [23] and also in the asymptotic evaluation of SIs [3], [4]. As the two halves of

the BCI path are on the same curve, it is convenient to form a new integrand that is the difference between the integrands on each half of the path. The integral is then a sum of the integral of this difference integrand and the contribution of an infinitesimal circle near the branch point. This last contribution turns out to be zero as can be seen by inspecting Tables I and II, and noting that the singularities at the branch points are at most of $O(1/\sqrt{|k_x - k^\pm|})$.

Turning to the integration of the difference integrand, we first obtain a parametric representation of the path of steepest descent away from the branch point, by the same method used in Section III. Denoting this parametric representation by $k_x^{\text{BC}}(\tau)$, it can be easily shown that the difference integrand will decay exponentially with τ when $|k_x^{\text{BC}}(\tau)| \gg \max(k^+, k^-)$, while at the branch point itself, it will have a $\sqrt{\tau}$ singularity. In accordance with this dependence on τ , we adopt a generalized Laguerre-Gaussian quadrature rule [32, p. 96] for which the corresponding weight function is $\sqrt{\tau} \exp(-\tau)$. Taking the $\sqrt{\tau}$ singularity into account in this way is a very simple method to deal with the integration of the singular integrand in an accurate and robust manner.

B. Transmitted Fields

As mentioned in Section III-A, when calculating the transmitted fields, there will always be a real saddle-point between the origin and the branch point associated with the thin medium. A SDP passing through this saddle point furnishes one contribution to the integral. This path will intercept the branch-point associated with the dense medium, whenever the path intercepts a second, complex, saddle point [31]. When this happens, a second SDP, that passes through the complex saddle point and surrounds the dense branch point must be added.

The physical significance of this contribution has been considered for line-source and beam excitations in [31], [33]. As explained in these references, this contribution has the ray-optical interpretation shown in Fig. 5. When the source is in the dense medium and the observation point is close to the interface, the contribution of the complex saddle-point corresponds to a ray originating at the source and reaching a point on the interface close to the observation point. This ray then proceeds to the observation point as an evanescent wave. Similarly, when the source is in the thin medium and it is close to the interface, an evanescent component of the plane wave spectrum of the line source reaches the interface and then proceeds to the observation point as a propagating wave.

The conditions for the inclusion of the complex saddle point contribution are as follows. Denoting by k_{sp}^r and k_{sp}^c the k_x values of the real and complex saddle points, respectively, the complex saddle point is intercepted whenever $\text{Re}[\alpha_t(k_{\text{sp}}^r)] < \text{Re}[\alpha_t(k_{\text{sp}}^c)]$. This condition is demonstrated in Fig. 6, where its correctness can be readily observed. The region in physical space which corresponds to the complex saddle point being intercepted is marked as region IV in Fig. 3. The lines delimiting region IV, in which the complex saddle point is intercepted, bear close resemblance to those of Fig. 1 in [31], where this region was sketched.

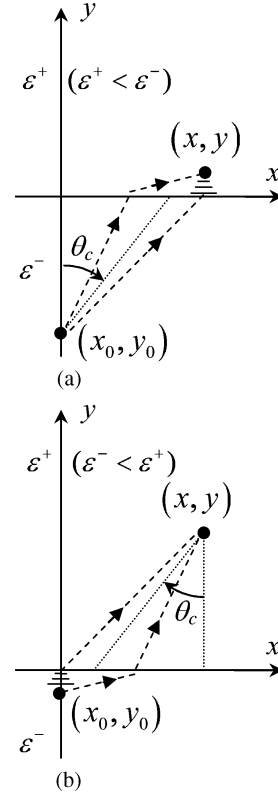


Fig. 5. Ray-optic interpretation of the contributions due to two saddle points. The real-line saddle point corresponds to the usual refracted ray, and the complex saddle point corresponds to a ray which is evanescent in the thin medium and propagating in the dense medium. In (a), the source is in the dense medium, whereas in (b), the source is in the thin medium.

V. CRITICAL ANGLE CASE

The saddle point for the reflected field is given by (17), from which it is evident that the saddle point for the reflected fields is found on a segment of the real axis in the k_x plane, between the origin and the branch point associated with the $y < 0$ region. When this region is the denser of the two, the saddle point and the branch point associated with the $y > 0$ region may coincide, as shown in Fig. 7. This happens when θ is equal to the critical angle defined by $\theta_c = \sin^{-1}(\sqrt{\epsilon_r^+/\epsilon_r^-})$. Although this branch point does not appear in α_u of the reflected field case, it does appear in the reflection coefficient $R(k_x)$, which is given by (6). As can be readily verified from (6), the reflection coefficient near the branch point at $k_x = k^+$ is approximately $1 + O(\sqrt{|k_x - k^+|})$. If the conventional Hermite-Gaussian quadrature rule is used, the rapid variation of the integrand near the branch point degrades the accuracy of the integration. This problem can be dealt with by use of a generalized Hermite-Gaussian quadrature rule [28, p. 32–33] for which the weight function is $\sqrt{\tau} \exp(-\tau^2)$. To obtain an integrand with this dependence, we first subtract and subsequently add a SI with a unit reflection coefficient. This SI can be evaluated analytically, as it is just the field of an image source which has the same amplitude as the original source. After subtracting the image source, if the saddle point and the branch point are close, but not exactly coincident, we shift the entire path laterally so that it is centered on the branch point. As long as the shift is

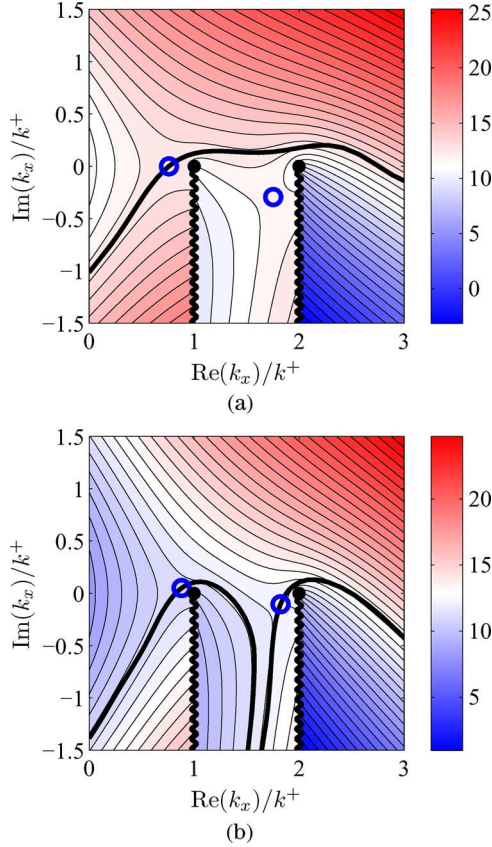


Fig. 6. The real part of the complex phase function of the transmitted fields, α_t , overlaid with contours of constant $\text{Re}(\alpha_t)$. In (a), the complex saddle point is not intercepted, whereas in (b) it is. The thick line shows the contour found by the algorithm, and the circle markers mark the saddle points.

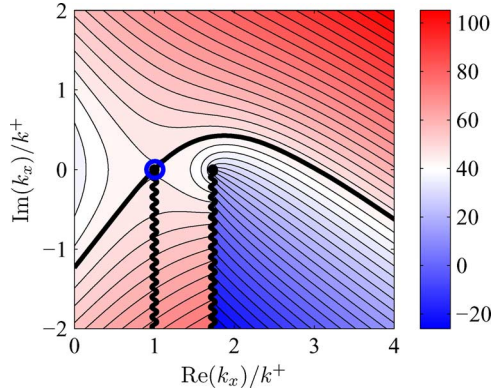


Fig. 7. Path for the critical angle case. The value shown is the real part of the complex phase function of the reflected fields, α_u , overlaid with contours of constant $\text{Re}(\alpha_u)$. The saddle point, marked by the circle marker, coincides with the branch point of the $y > 0$ region.

small, the behavior of the integrand on the path will not be altered significantly, except in the neighborhood of the branch point, where it will have a square-root singularity. The generalized Hermite-Gaussian quadrature rule can now be applied to the integrand on the shifted path.

A reasonable criterion for the use of this technique is that the branch point be contained in a neighborhood of the saddle point,

the size of the neighborhood being some effective radius of the saddle point region. We found, empirically, that a good effective radius is σ , the standard deviation of the Gaussian envelope of the integrand, given by (27). To summarize the procedure, we represent the fields reflected at the critical angle by a sum of the fields due to an image source and a correction term which can be integrated readily, on a slightly shifted path, by the generalized Hermite-Gaussian quadrature rule.

VI. GRAZING ANGLE CASE

When $\theta \approx \pi/2$, or equivalently, $|x - x_0| \gg |y| + |y_0|$, the saddle point(s) approach the branch point(s), and this makes the integration more difficult. In the evaluation of the reflected field, the saddle point approaches the branch point at $k_x = k^-$. In the evaluation of the transmitted field, two saddle points are relevant [31]. The real transmitted-field saddle-point approaches the branch point at $k_x = k^{\text{th}}$, and the complex transmitted-field saddle-point approaches the branch point at $k_x = k^{\text{dn}}$. As a saddle point approaches a branch point, the integrand along the corresponding SDP becomes more difficult to integrate due to the proximity of the singularity. Also, the path bends more tightly around the branch point, and the contours of steepest-descent become aligned with the imaginary k_x axis. Consequently, the integration along the SDP takes the form of a branch-cut integration around a vertical branch-cut. Branch cut integrals are common in the SI literature. However, the method usually employed for their evaluation, namely, integration along the path of steepest descent beginning from the branch point [3], [4], [20], [23], can only be applied in the reflected field case and only for the BCI around the branch point at $k_x = k^+$, marked by BCI₁ in Fig. 8(a). It cannot be applied to the other BCIs because in these cases the complex phase function is singular at the branch point to be surrounded, and therefore no path of steepest-descent passing through the branch point exists.

To overcome the above mentioned difficulty, we propose to calculate each BCI on a path that is made-up of two infinitesimally close, straight parallel lines, and an infinitesimal circle around the branch point. These keyhole-like paths are shown in Fig. 8(a) (marked BCI₂) for the reflected fields, and in Fig. 8(b) for the transmitted fields. The integrand along these paths becomes singular at the branch point when the radius of the circle and the distance between the straight lines vanish. The order of the singularity, however, is determined solely by which field component is being calculated, and it does not depend on the distance of the saddle point from the branch point. It can therefore be dealt with, in a very robust manner, by including it in the weight function of the Gaussian quadrature rule.

The orientations of the keyhole paths are determined by the following considerations. As can be observed in Fig. 8, the contours of steepest descent tend to become parallel away from the branch points. The limiting values of the slopes of the contours as $|k_x|/k^{\text{dn}} \rightarrow \infty$ can be readily derived by noting that in this limit, $k_y^- \approx j\hat{\sigma}^-k_x$ and $k_y^+ \approx j\hat{\sigma}^+k_x$, where $\hat{\sigma}^+$ and $\hat{\sigma}^-$ are either $+1$ or -1 depending on the Riemann-sheet. For example, to calculate the asymptotic slopes on the proper Riemann-sheet,

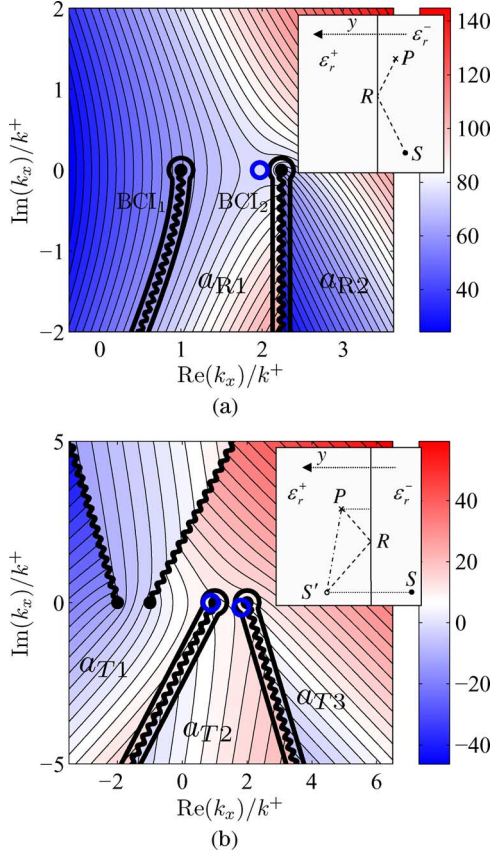


Fig. 8. BCI paths for, (a) the reflected, and (b) the transmitted fields, in the grazing angle case. In the insets, geometrical interpretations of the asymptotic slopes given by (30) and (31) are shown. The source point is labeled S , its image is labeled S' , the observation point is labeled P , and the point of specular reflection is labeled R . In (a), the slopes of the lines SR and RP with respect to the interface are equal to the asymptotic slopes a_{R1} and a_{R2} , respectively. In (b) the slopes of the lines $S'R$, $S'P$, and RP , are equal to a_{T1} , a_{T2} , and a_{T3} , respectively.

both $\hat{\sigma}^-$ and $\hat{\sigma}^+$ are taken to be $-\text{sgn}[\text{Re}(k_x)]$. The asymptotic slopes, a , are then given, with the notation of (12), (13), by

$$a = \frac{|x - x_0|}{\hat{\sigma}^- y^- + \hat{\sigma}^+ y^+}. \quad (29)$$

By specializing (29) to the case of the reflected fields, we find that the asymptotic slopes are given by

$$a_{R1} = |x - x_0| / (|y_0| + |y|) \quad (30a)$$

$$a_{R2} = -a_{R1}. \quad (30b)$$

The asymptotic slopes have a simple geometrical interpretation shown in the inset of Fig. 8(a). Similarly, by specializing (29) to the case of the transmitted fields, we find that the asymptotic slopes are given by

$$a_{T1} = |x - x_0| / (y^+ + y^-) \quad (31a)$$

$$a_{T2} = \text{sgn}(\varepsilon_r^- - \varepsilon_r^+) |x - x_0| / (y^- - y^+) \quad (31b)$$

$$a_{T3} = -|x - x_0| / (y^+ + y^-) \quad (31c)$$

where the regions for which the asymptotic slopes are a_{T1} , a_{T2} , and a_{T3} are indicated in Fig. 8(b). These slopes too have simple geometrical interpretations that are shown in the inset of Fig. 8(b). If the slope of the branch cut and the path were taken equal to one of the asymptotic slopes, the integrand would oscillate slowly on one half of the path, but then it would oscillate rapidly on the other half. Since the accuracy of the integration is determined by the fastest variation along the path, we choose the slope of the branch cut so as to minimize the oscillation rate of the integrand. This corresponds to choosing the branch cut and the path on the bisector of the angle between two lines having asymptotic slopes. Lastly, choosing the keyhole path in the lower half of the complex k_x plane guarantees that the contribution of the segments used to connect the two BCI paths to the original path and to each other at infinity is zero.

A. Gaussian Quadrature Rule

As the two halves of the keyhole paths coincide with the branch cut, it is convenient to form a new integrand that is the difference between the integrand evaluated on each side of the branch cut. The integral is then a sum of the integral of this difference integrand and the contribution of the infinitesimal circle, which turns out to be zero. To evaluate the integral, we express the keyhole paths beginning at $k_x = k^\pm$ by the following parametric representations

$$k_x^\pm(\tau) = k^\pm (1 + \tau e^{j\phi^\pm}), \quad 0 \leq \tau \leq \infty \quad (32)$$

where the angle between the positive real k_x axis and the path is denoted by ϕ^\pm . The integration with respect to τ can now be effected by Gaussian quadrature.

The choice of the Gaussian quadrature rule is dictated by the behavior of the difference integrand along the keyhole path. This integrand decays exponentially with τ when $|k_x^\pm(\tau)| \gg k^{\text{dn}}$, while at the branch point itself, it has a $\sqrt{\tau}$ or $1/\sqrt{\tau}$ singularity. In accordance with this dependence on τ , we adopt a generalized Laguerre-Gaussian quadrature rule for which the corresponding weight function is $\tau^{\pm 0.5} \exp(-\tau)$.

In this weight function, the exponent of τ must be set according to the singularity of the difference integrand at the branch point. By use of Tables I and II it can be determined that the exponent should always be set to $+0.5$ except when calculating the z or y components of the reflected electric or magnetic fields; in these cases, the exponent should be set to -0.5 .

B. Criterion for the Use of the Keyhole Paths

As the specular reflection angle θ approaches $\pi/2$, the integration along the keyhole paths becomes more accurate. This is because the asymptotic slopes and the slope of the path all become aligned, thus making the integrand slowly oscillating on the path. When the source and observation points recede from the interface, the accuracy of the integration along the keyhole path deteriorates, but then the usual SDPs can be used because the saddle points move away from the branch points. A criterion we found to be simple and reliable is to use the SDP whenever the distance of the saddle point from the branch point, $|k^\pm - k_{\text{sp}}|$,

is greater than the standard deviation of the Gaussian envelope of the integrand σ , given by (27), and to use the keyhole path otherwise.

C. High Contrast

When $\varepsilon_r^{\text{dn}} \gg \varepsilon_r^{\text{th}}$, the evaluation of the fields of a ELS does not present any special difficulties. The MLS case, however, is complicated by the presence of a leaky pole near the branch point at $k_x = k^{\text{th}}$. This follows from examination of the expressions for the reflection and transmission coefficients given in (6). The denominator of $R(k_x)$ is never zero in the ELS case, but in the MLS case $R(k_x)$ has a pole at $k_x = k_p$, where

$$k_p = k_0 \sqrt{\frac{\varepsilon_r^{\text{dn}} \varepsilon_r^{\text{th}}}{\varepsilon_r^{\text{dn}} + \varepsilon_r^{\text{th}}}} \quad (33)$$

and k_0 is the free-space wave number. This pole is leaky, as it occurs only in the two improper Riemann sheets defined by $\text{Im}(k_y^+) > 0$, $\text{Im}(k_y^-) < 0$ and $\text{Im}(k_y^-) < 0$, $\text{Im}(k_y^+) > 0$. The leaky pole is never intercepted by the keyhole paths, but the accuracy of the integration will deteriorate if the pole is close to a path. From (33), it follows that this pole is constrained to the segment of the real axis between the origin and the branch point at $k_x = k^{\text{th}}$. As the contrast increases, the pole approaches the branch point at $k_x = k^{\text{th}}$. A keyhole path surrounding this branch point will penetrate into the improper sheet that contains the leaky pole, and consequently, accuracy will be poor if this path is used.

To overcome this problem, we use a singularity subtraction technique similar to that employed in the *modified saddle-point technique* [34, pp. 615–620]. In this well-known technique, the singular term is subtracted from the integrand, and then added back after its integral along the SDP is written in terms of the error function, $\text{erf}(x)$. In this work, the path of integration is the keyhole path and not the SDP, but nevertheless, the integral along the keyhole path can also be written in terms of the error function.

Let us denote by $D(\tau)$ the difference integrand evaluated on the keyhole path given by (32), as function of the parametric variable τ . The function $D(\tau)$ has the following properties.:

- It has a simple pole at $\tau = \tau_p$, where from (32),

$$\tau_p = e^{-j\phi^{\text{th}}} \left(\frac{k_p}{k^{\text{th}}} - 1 \right). \quad (34)$$

Here ϕ^{th} is the angle of the path that surrounds the branch point associated with the thin medium.

- It decays exponentially when $\tau \rightarrow \infty$, with an attenuation constant denoted by γ^{th} .
- When $\tau \rightarrow 0$ it is $O(\tau^{\pm 0.5})$, the sign depending on the component being calculated, as explained in the last paragraph of Section VI-A.

The integral to be evaluated, $\int_0^\infty D(\tau) d\tau$, can be written as the sum of two terms: an integral of a regular function, I_{reg} , and an integral of a singular term, I_p , as follows:

$$\int_0^\infty D(\tau) d\tau = I_{\text{reg}} + I_p \quad (35)$$

$$I_{\text{reg}} = \int_0^\infty \left[D(\tau) - g_p \frac{\tau^{\pm 0.5} e^{-\gamma^{\text{th}} \tau}}{\tau - \tau_p} \right] d\tau \quad (36)$$

$$I_p = g_p \int_0^\infty \frac{\tau^{\pm 0.5} e^{-\gamma^{\text{th}} \tau}}{\tau - \tau_p} d\tau \quad (37)$$

$$g_p = \lim_{\tau \rightarrow \tau_p} \frac{(\tau - \tau_p)}{\tau^{\pm 0.5} e^{\gamma^{\text{th}} \tau}} D(\tau). \quad (38)$$

The integrand in (36) is regular at $\tau = \tau_p$, and it behaves asymptotically the same as $D(\tau)$ when $\tau \rightarrow 0$ and $\tau \rightarrow \infty$. Hence, the generalized Gauss-Legendre rule specified in Section VI-A can be used for its integration with confidence. The second term, I_p , can be evaluated by use of the error function. If the exponent of τ in (37) is $+0.5$, we have

$$I_p = g_p \left[\sqrt{\frac{\pi}{\gamma^{\text{th}}}} - \frac{j\pi\sqrt{\tau_p} \text{erf}(-j\sqrt{\gamma^{\text{th}} \tau_p}) - \pi\sqrt{-\tau_p}}{e^{\gamma^{\text{th}} \tau_p}} \right] \quad (39)$$

and if the exponent of τ is -0.5 , we have

$$I_p = -g_p \frac{\pi}{\sqrt{\gamma^{\text{th}} \tau_p}} e^{-\gamma^{\text{th}} \tau_p} \left[j + j \text{erf}(-j\sqrt{\gamma^{\text{th}} \tau_p}) \right]. \quad (40)$$

In (39), (40), the principal branch of the square-root should be used.

We consider a case to be one of high-contrast if and only if $|x - x_0| < 1/|k_p - k^{\text{th}}|$. The reason that the keyhole paths can be used if $|x - x_0| > 1/|k_p - k^{\text{th}}|$ is that the integrand along these paths decays exponentially, with an attenuation constant which is approximately $|x - x_0|$. So if $|x - x_0| > 1/|k_p - k^{\text{th}}|$, the integrand will decay rapidly on the keyhole paths compared to the variation due to the nearby branch point.

D. Low Contrast

When $\varepsilon_r^- \approx \varepsilon_r^+$, the critical angle approaches $\pi/2$ so the critical angle case and the grazing angle case merge. This situation is of considerable interest, among other things, as an approximation to continuous stratification (see [35, p. 25–32] and references therein). The keyhole paths and Gaussian quadrature rules described in this section are inadequate in the low-contrast case. The Gaussian quadrature rule takes into account the singularity that the path surrounds, but not the other singularity, which, when the contrast is low, is nearby. To solve this problem, instead of using two keyhole paths, one around each branch point, we use one path that surrounds both of them at a prudential distance. The path, shown in Fig. 9, is made up of a semicircle of radius R_{LC} and two straight lines which begin on the real line and their slopes are the asymptotic slopes of (29)–(31). The integration along the straight lines is performed,

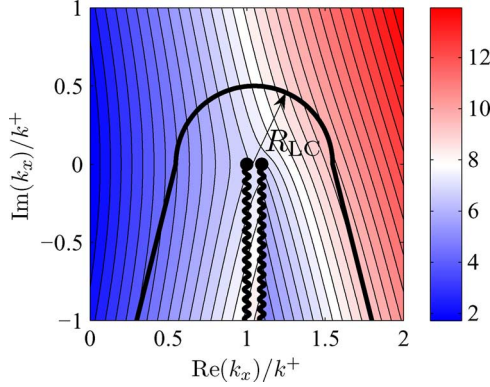


Fig. 9. Path for the low contrast case. The value shown is the real part of the complex phase function α_u , overlaid with contours of constant $\text{Re}(\alpha_u)$.

similarly to the integration on the keyhole paths, by a (non-generalized) Laguerre-Gaussian quadrature rule. The integration along the semicircle is performed by a Legendre-Gaussian quadrature rule. The number of integration points is divided equally between the semicircle and the straight lines.

The radius of the semicircle, R_{LC} , is chosen as follows. On the one hand, the radius should be large enough so as to avoid the branch points. On the other hand, if the radius is too large, the number of oscillations of $\exp[-j\alpha_u(k_x)]$ along the semicircular path will be proportionately large, and this will require a finer integration along the semicircle. In the grazing angle case, we can make the approximation $\exp[\alpha_u(k_x)] \approx \exp(-j|x - x_0|k_x)$, from which it can be deduced that letting $R_{LC} = \pi/|x - x_0|$ ensures that only one period of $\exp(-j|x - x_0|k_x)$ fits into the semicircle. Still, it may not appear evident that this radius is large enough. Indeed, as $|x - x_0|$ increases, the semicircle shrinks towards the branch points. It turns out, however, that if this occurs, it is possible to revert to the keyhole paths proposed earlier. We therefore consider a case to be one of low contrast if and only if $|x - x_0| < 1/|k^+ - k^-|$. Like in the high-contrast case, the reason that the keyhole paths can be used if $|x - x_0| > 1/|k^+ - k^-|$ is that the integrand along these paths decays exponentially, with an attenuation constant which is approximately $|x - x_0|$. So if $|x - x_0| > 1/|k^+ - k^-|$, the integrand will decay rapidly on the keyhole paths compared to the variation due to the nearby branch point.

VII. THE QUASI-STATIC CASE

It is well-known that in the quasi-static case the exponential factor $\exp[-j\alpha_u(k_x)]$ in (3) varies more slowly than the other factors, denoted collectively by $F(k_x)$. As detailed in Tables I and II and in (6) and (10), the factor $F(k_x)$ is the product of a reflection or transmission coefficient, and an amplitude function that depends on the field component being evaluated and on whether the source is an ELS or an MLS. The relationship between the various factors is more clear when they are written in terms of a normalized integration variable, $\xi = k_x/k_0$. The exponential factor is then given by

$$\exp[-j\alpha_u(\xi)] = \exp[-jk_0(|x - x_0|\xi + y^-\sqrt{\varepsilon_r^- - \xi^2} + y^+\sqrt{\varepsilon_r^+ - \xi^2})] \quad (41)$$

the reflection coefficient by

$$R(\xi) = \begin{cases} \frac{\sqrt{\varepsilon_r^- - \xi^2} - \sqrt{\varepsilon_r^+ - \xi^2}}{\sqrt{\varepsilon_r^- - \xi^2} + \sqrt{\varepsilon_r^+ - \xi^2}} & \text{for ELS} \end{cases} \quad (42a)$$

$$\begin{cases} \frac{\varepsilon_r^+ \sqrt{\varepsilon_r^- - \xi^2} - \varepsilon_r^- \sqrt{\varepsilon_r^+ - \xi^2}}{\varepsilon_r^+ \sqrt{\varepsilon_r^- - \xi^2} + \varepsilon_r^- \sqrt{\varepsilon_r^+ - \xi^2}} & \text{for MLS} \end{cases} \quad (42b)$$

and the transmission coefficient by $T(\xi) = 1 + R(\xi)$. The amplitude functions can all be written as

$$A(\xi) = \frac{N(\xi)}{\sqrt{\varepsilon_r^- - \xi^2}} \quad (43)$$

where $N(\xi)$ is either 1, ξ , or $\sqrt{\varepsilon_r^\pm - \xi^2}$. Clearly, when $(|x - x_0| + |y^+| + |y^-|)k_0 \rightarrow 0$, the variation of $\exp[-j\alpha_u(\xi)]$ with ξ becomes negligible, whereas that of the other factors, $R(\xi)$, $T(\xi)$ and $A(\xi)$ is unaffected.

Naturally, a Gaussian quadrature rule that is tailored to the variation of the exponential factor is inadequate in this situation. It is more reasonable to use a Gaussian quadrature rule that is tailored to the variation of $F(\xi)$ and to assume that the exponential factor is slowly varying. If $F(\xi)$ decays to zero quickly as $|\xi| \rightarrow \infty$, the main contribution to the integral will come from a small region in the ξ plane, and, as the exponential factor will not vary significantly in this region, a small number of integration points will yield good accuracy. In some cases, however, the function $F(\xi)$ does not decay to zero, or it decays very slowly, as $1/|\xi|$. To see this, note that $F(\xi)$ is the product of $R(\xi)$ or $T(\xi)$ by the appropriate $A(\xi)$. The amplitude function $A(\xi)$ decays, if at all, no faster than $1/|\xi|$, while, in some cases, $R(\xi)$ and $T(\xi)$ do not decay at all. For example, in the ELS case, $R(\xi) \propto 1/|\xi|^2$ when $|\xi| \rightarrow \infty$, but then $T(\xi) \rightarrow 1$. In the MLS case, neither $R(\xi)$ nor $T(\xi)$ decay to zero. This problem can be remedied by subtracting from $R(\xi)$ or $T(\xi)$ their limiting value as $|\xi| \rightarrow \infty$, as is done in the DCIM [12]. The subtracted term can be added after analytical integration as it corresponds to the field of a line-source placed either at the image point (for the reflected field) or at the source point (for the transmitted field). After the subtraction, the remaining factor, denoted $\tilde{F}(\xi)$, decays at least as fast as $1/|\xi|^2$.

A. Integration Path

The path is chosen according to the following guidelines.

- The contributions due to segments connecting the ends of the path with the ends of the original path P should be zero. This implies that the path should start and end on the proper sheet, in the lower half of the complex k_x plane.
- The path should steer away as much as possible from the branch points, and it should not intercept them.
- The path should not venture too high-up into the upper half of the complex k_x plane, as the integrand can grow exponentially when $\text{Im}(k_x) \rightarrow \infty$.

These guidelines lead us to choose a parabolic path [shown in Fig. 10(a)] that crosses the real line at $k_x = 0$ and $k_x = 2k^{\text{dn}}$, at 45° angles. Passing through $k_x = 0$ ensures that the path does not pass close to the branch points at $k_x = \pm k^{\text{th}}$, while passing through $k_x = 2k^{\text{dn}}$ ensures that it does not pass close to the branch point at $k_x = k^{\text{dn}}$. The 45° angles are a compromise

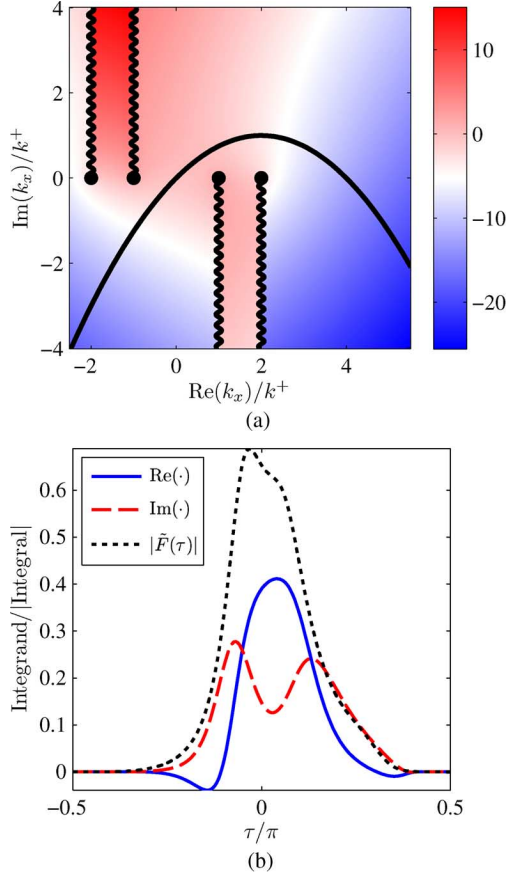


Fig. 10. Integrand and path in the quasi-static case. In (a), the value shown is the amplitude of the transmitted E_z integrand in dB above its value at $k_x = 0$. In (b), the real and imaginary parts of the integrand are shown, together with the weight function $|\tilde{F}(\tau)|$, on the proposed path. The plots are normalized by absolute value of the integral.

between going too high into the upper half plane and passing too near the branch points. The equation for this path is given by

$$\text{Im}(k_x) = -\frac{\text{Re}(k_x) [\text{Re}(k_x) - 2k^{\text{dn}}]}{2k^{\text{dn}}}. \quad (44)$$

To derive the Gaussian quadrature rule, it is convenient to replace this equation by a parametric representation of the path such that a finite range of the parametric variable, τ , spans it entirely. To this end, a transformation similar to the one in [10] is used. We have

$$\text{Re}[k_x(\tau)] = k^{\text{dn}} \tan \tau, \quad -\pi/2 < \tau < \pi/2 \quad (45)$$

which, when substituted into (44), yields

$$k_x(\tau) = k^{\text{dn}} \tan \tau \left[1 - j \frac{1}{2} (\tan \tau - 2) \right]. \quad (46)$$

A Gaussian quadrature rule can now be derived for the integrand on the finite range of τ .

B. Gaussian Quadrature Rule

In Fig. 10(b) a typical quasi-static case integrand is shown together with $|\tilde{F}(\tau)|$ on the proposed path, as a function of a parametric variable τ . Once the path and the permittivities have been set, the function $|\tilde{F}(\tau)|$, which remains the same for all source and observation points, is used as the weight function of the Gaussian quadrature rule.

To obtain this rule, we use a discretization method [28]. In discretization methods, a positive weight function, say $w(\tau)$, is replaced by a discrete weight function $w_N(\tau) = \sum_{k=0}^N w(\tau_k) \delta(\tau - \tau_k)$, where the sampling points τ_k are distributed on the support of $w(\tau)$, and $\delta(\cdot)$ is the Dirac delta function. Deriving a Gaussian quadrature rule for $w_N(\tau)$ is much more simple than deriving such a rule for $w(\tau)$ because the difficult step in the derivation is the evaluation of the moments of the weight function, $\int \tau^n w(\tau) d\tau$, and for $w_N(\tau)$ this is trivial. It can be shown, that for any weight function that has finite moments of all orders, the integration points and weights obtained in this way converge to those of the Gaussian quadrature rule for $w(\tau)$, as $N \rightarrow \infty$ [28, p. 91]. In this work, we used Gautchi's implementation of this technique, which is freely available [36].

Lastly, it is important to note that while $\tilde{F}(\xi)$ depends on the permittivities, it does not depend on the source or observation points. Therefore, for given permittivities, the same integration path and Gaussian quadrature rule can be used for all source and observation points belonging to the quasi-static case.

C. Criterion for the Quasi-Static Case

We use the quasi-static case method when the variation of $\exp[-j\alpha_u(\xi)]$ is slow enough so that its period in the ξ plane is larger than the effective width of the envelope function $\tilde{F}(\xi)$. To find the period of $\exp[-j\alpha_u(\xi)]$, we note that the oscillations of this function are most rapid in the direction perpendicular to that of steepest descent, and they are fastest when $|\xi| \rightarrow \infty$. In this limit, the smallest oscillation period, Λ , is given by

$$\Lambda = \frac{1}{\sqrt{(x - x_0)^2 + (|y| + |y_0|)^2}} \frac{2\pi}{k_0}. \quad (47)$$

Since the envelope function starts to decay as fast as $1/|\xi|^2$ when $|\xi| \gg \sqrt{\varepsilon_r^{\text{dn}}}$, we use the quasi-static method whenever $\Lambda > 2\varepsilon_r^{\text{dn}}$. Rephrased in a more physically meaningful form, this condition reads $\lambda^{\text{dn}} / \sqrt{(x - x_0)^2 + (|y| + |y_0|)^2} > 2$, where λ^{dn} is the wavelength in the denser medium.

VIII. NUMERICAL RESULTS

Sommerfeld integral evaluation techniques have to cope with a wide range of problem parameters. These are: the coordinates of the source and observation points, the material parameters, the type of source, and the field component being calculated. The behavior of the integrands, and the physics underlying this behavior, change significantly with the problem parameters. It therefore seems inevitable that only an amalgam of various techniques can efficiently yield accurate results across the parameter

domain. In this section, the performance of the techniques described in this paper, which we collectively term the ND-SDP method, will be charted.

Throughout this section, we will show how the relative error of the numerical integration, Δ , varies with the parameters of the problem and the algorithm. To calculate this error, we need the exact value of the integral, which, of course, is unavailable. To approximate the exact value, we use adaptive Gauss-Kronrod integration along a path which follows the real axis and is slightly indented into the first and third quadrants. This path, taken from [10], has the following parametric representation:

$$k_x(\tau) = k'(\tan \tau + j\gamma\tau) \quad -\pi/2 < \tau < \pi/2 \quad (48)$$

where

$$k' = \begin{cases} \frac{k^+ y_0 - k^- y}{y_0 - y} & y \leq 0 \\ k^+ & y > 0 \end{cases} \quad (49a)$$

$$(49b)$$

$$\gamma = \min \left\{ 1, [k'(x - x_0)]^{-1} \right\}. \quad (50)$$

The adaptive integration is stopped when it has converged to machine precision.

In Fig. 11(a), the relative error in the computation of the reflected and transmitted E_z fields is shown on a logarithmic scale. These fields are due to an ELS at $x_0 = 0$, $y_0 = -\lambda$, λ being the free-space wavelength. The various paths used in each region are also indicated. Some of the paths, such as those labeled 1, 4, and 5, consist of a single curve, whereas the rest of the paths consist of two curves. The integrand is evaluated m times along each curve, so the evaluation in regions 1, 4 and 5, is two times faster than the evaluation in the other regions. In this example $m = 20$. A plot similar to the one shown in Fig. 11(a) is shown in Fig. 11(b). The only difference between these figures is that in the latter the ELS is closer to the interface ($y_0 = -\lambda/100$), and the range of the observation coordinates is smaller. This is done to show the calculation errors in the quasi-static case (region 2) and in the low-contrast grazing angle case (region 4). As can be readily observed in Fig. 11, with $m = 20$, the largest error is less than 1% (it is 0.0058), and in most regions the error is much smaller. Even smaller errors can be obtained by increasing m . This can be seen in Fig. 12(a), where the dependence of $\log_{10} \Delta$ on m is plotted, for representative observation points taken from each region in Fig. 11(a). Similarly, for representative points in Fig. 11(b), the corresponding plot of $\log_{10} \Delta$ vs. m is shown in Fig. 12(b). For all regions, the plots imply convergence, approximately at an exponential rate. For some regions, like 1–4 in Fig. 11(a), the convergence is extremely fast, the results reaching machine precision with 20–40 samples. In other regions, like 5 in Fig. 11(b), the numerical integration converges more slowly. However, as can be seen in Fig. 12(b) for the point from region 5, convergence with less than 10^{-6} relative error is achieved with as few as 25 samples.

An important advantage of using Gaussian quadrature, as opposed to more elaborate integration techniques such as those used in the DCIM, is that the computation time scales linearly with the number of integrand samples. This can be observed in Fig. 13, where the computation times on a 3 GHz PC for the

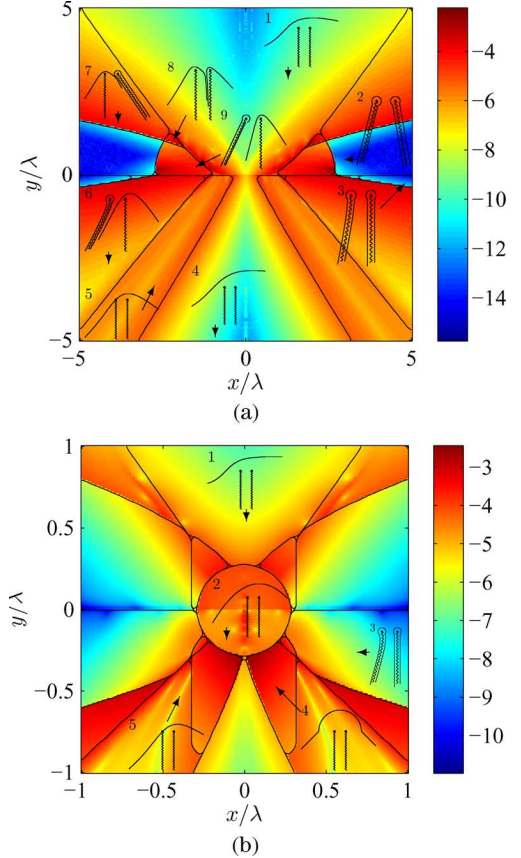


Fig. 11. Relative error on a logarithmic scale, $\log_{10} \Delta$, as function of observation coordinates x and y . The fields computed are the transmitted and reflected E_z fields due to an ELS at $x_0 = 0$ and: (a) $y_0 = -\lambda$, (b) $y_0 = -\lambda/100$. The relative permittivities are $\epsilon_r^- = 3$ and $\epsilon_r^+ = 1$.

representative points of Fig. 11(a) are shown. Times shown are for the evaluation of a single integral with the time required for initialization (less than 1 sec) deducted. As can be inferred from these plots, fairly high accuracy can be obtained in less than 1 msec per evaluation by using, say, 40 sampling points. At the other end, very high accuracies (approaching machine precision) can be obtained by investing just a few milliseconds per evaluation.

The numerical results presented so far indicate that the accuracy obtained for a given m varies considerably with the problem parameters. To obtain a more comprehensive picture of this variation, we tested the algorithm on a large number (100000) of cases with randomly selected parameters, and $m = 20$. The range of parameters is given in the table in Fig. 14, together with a histogram of the relative errors. As expected, the range of relative errors is very large, spanning about 14 orders of magnitude. Like in Fig. 11, the largest relative error is less than 0.006. The various paths used in the algorithm generally yield more accurate results as the distance between the source and observation points increases. Hence, increasing the range of the coordinates would lower the errors.

A. An Adaptive Integration Scheme

The median of the $\log_{10} \Delta$ distribution shown in Fig. 14 is 2.1×10^{-11} . As $m = 20$, this small error implies that remarkably high accuracy can be attained at a modest computational

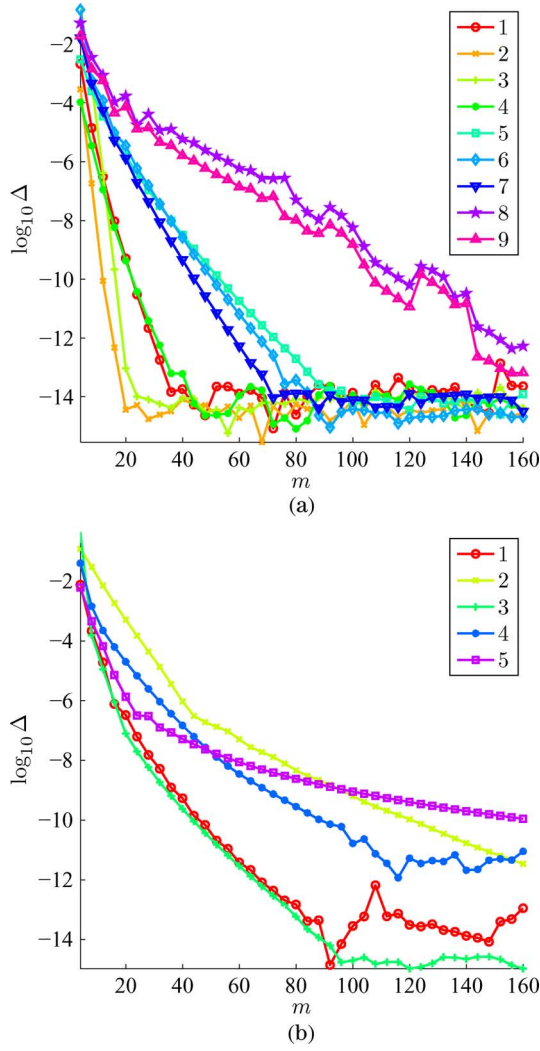


Fig. 12. Relative error, Δ , on a logarithmic scale, vs. m , for representative points taken from: (a) regions 1–9 in Fig. 11(a), and (b) regions 1–5 in Fig. 11(b).

cost. Nevertheless, the large variation in the relative errors for a constant m may appear disadvantageous. If some minimum accuracy is required, m has to be taken large, even though for many cases a much smaller number would suffice. A simple solution to this problem is to vary m adaptively, increasing it until the results have converged to a given tolerance. It should be noted, that if many integrals are to be computed, m should be kept constant for as many cases as possible, as changing m requires recalculation of the matrices $[V]$ and $[V]^+$ defined in (25), (26). In our implementation, we start by computing all integrals with $m = 8$ and $m = 16$. All integrals for which the difference between these two calculations is greater than the tolerance are recalculated with $m = 32$. We continue multiplying m by 2 until all integrals have converged to the specified tolerance. It may seem natural to use a Gauss-Kronrod-type extension rule in order to reuse the integrand samples when increasing m . Unfortunately, however, as proved in [37], such extensions of the Gauss-Laguerre and Gauss-Hermite rules do not exist. The results of applying the adaptive scheme to the same problem of Fig. 11(a), with a tolerance of 10^{-4} , are shown in Fig. 15. In

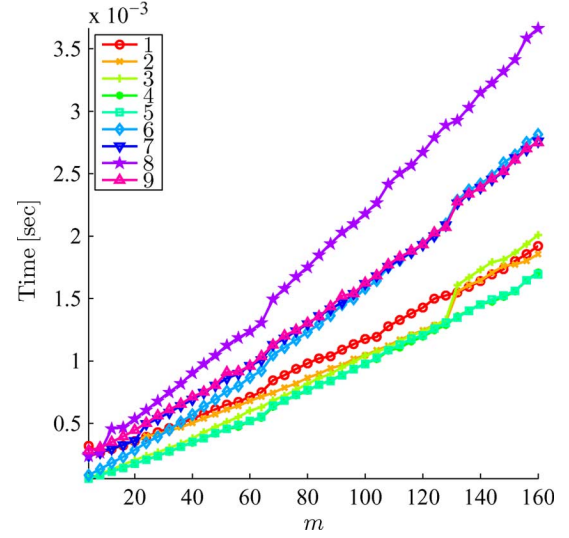
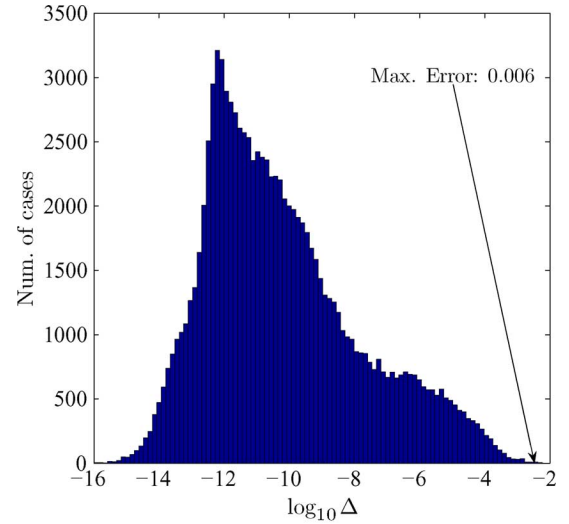


Fig. 13. Computation time vs. m for the representative points used in Fig. 12(a), on a 3 GHz PC.



Parameter	Range
$x - x_0, y, y_0$	$[-10\lambda, 10\lambda]$
$\varepsilon_r^-, \varepsilon_r^+$	$[1, 10]$
Source type	ELS MLS
Field component	E_z H_z

Fig. 14. Histogram of relative errors obtained by testing the algorithm on 100000 integrals, with the problem parameters chosen randomly. The range of parameters is given in the table.

Fig. 15(a), the relative error is shown, on a logarithmic scale, and as can be readily observed, the largest error is indeed below the tolerance. In Fig. 15(b), the value of $\log_2 m$ at which the algorithm stopped for each observation point is shown. In a vast majority of observation points, the integrals converged in the first or second steps, i.e., with $\log_2 m = 4$ or $\log_2 m = 5$. A few points, however, required $\log_2 m = 7$. It should be noted that, for each point, the integrals must be calculated with all m

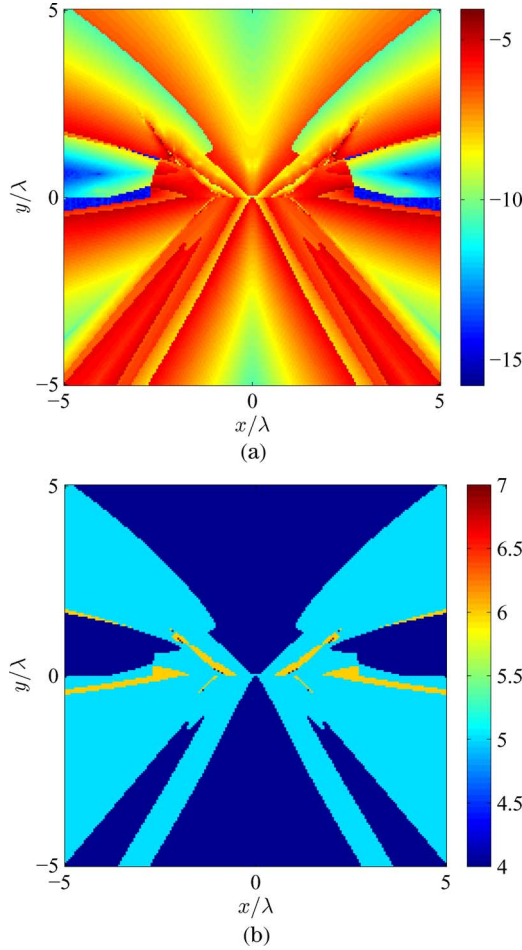


Fig. 15. In (a), the relative error, on a logarithmic scale, obtained with by adaptively modifying m . In (b), the value of $\log_2 m$ at which the adaptive algorithm stopped. All problem parameters are the same as those of Fig. 11(a).

values preceding the value shown. Therefore, the number of integrand evaluations for each point is given by

$$\sum_{i=3}^m 2^i = 2^{m+1} - 8 \quad (51)$$

This means that a plot of the total number of integrand evaluations for each point would look approximately the same as the plot of Fig. 15(b), shifted upwards by one unit of $\log_2 m$. The average computation time per point in this example is 9.5 msec, which is far less than it would take to compute all points with the maximum m , i.e., $m = 2^7$.

B. Solution of a Simple Scattering Problem

The research into efficient evaluation of SIs is chiefly motivated by integral-equation formulations of scattering problems. Below, we show an example of the application of the SI evaluation techniques presented in this paper to the solution of a simple scattering problem. This problem has been solved in the past, and by comparing our results with the previous data we are able to partly validate our code. The solution of the scattering problem is effected by use of the source-model technique (SMT) [38], which belongs to the method of moments (MoM) class of techniques. What sets the SMT apart from more con-

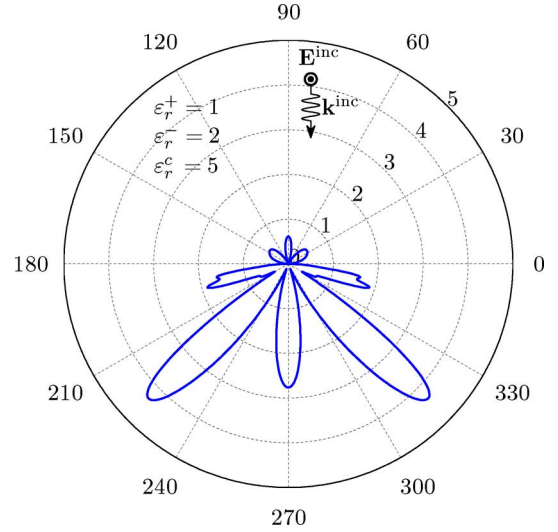


Fig. 16. Scattering width of a half-buried dielectric cylinder of radius $r = 0.5\lambda$ and relative permittivity $\epsilon_r^c = 5$. As the incidence is normal, $\mathbf{k}^{\text{inc}} = -k_0 \mathbf{u}_y$. The scattering width is normalized to the free-space wavelength λ .

ventional MoM techniques is that the current sources are elementary sources and they are placed at a small distance from the media boundaries and not right on them. In this way, the integration of the Green's function, required when the basis functions are continuous current sources, is obviated. The SMT has been used to solve a wide range of electromagnetic problems [39]–[44] and is a viable alternative to more conventional MoM techniques. It has been used previously, in [10], to analyze scattering from cylinders in the presence of a dielectric half-space. Here, we followed the formulation given in [10], but replaced the SI evaluation routine with the present one, and reproduced all the numerical results given there with high-fidelity. One of these results is shown in Fig. 16. The problem analyzed is that of scattering by a circular dielectric cylinder, which is half-buried in a dielectric half-space. The cylinder is illuminated by a TM plane wave, the electric field of which is given by

$$\mathbf{E}^{\text{inc}} = \mathbf{u}_z \exp[-j\mathbf{k}^{\text{inc}} \cdot (x\mathbf{u}_x + y\mathbf{u}_y)] \quad (52)$$

where \mathbf{u}_x , \mathbf{u}_y and \mathbf{u}_z are unit vectors, and \mathbf{k}^{inc} is the wave vector. The radius of the cylinder is $r = 0.5\lambda$, its relative permittivity is $\epsilon_r^c = 5$, and its axis coincides with the z axis. The region above the cylinder is air ($\epsilon_r^+ = 1$) and the region below the cylinder is characterized by a relative permittivity $\epsilon_r^- = 2$. The polar plot in Fig. 16 shows the (angle-dependent) scattering width, $W_{2D}(\phi)$, defined by

$$W_{2D}(\phi) = \lim_{\rho \rightarrow \infty} 2\pi\rho \frac{|\mathbf{E}^s|^2}{|\mathbf{E}^{\text{inc}}|^2} \quad (53)$$

where \mathbf{E}^s denotes the scattered electric field, and ϕ denotes the azimuthal angle. In [10], the polar plot was validated by comparing it with the results of [45], in which this problem was also studied, and good agreement was observed.

To solve the scattering problem, we used 80 basis functions: 40 electric line sources for the fields outside of the cylinder, and

TABLE IV
COMPARISON OF COMPUTATION TIMES ON A 3 GHz PC

	Method of [10] (sec)	ND-SDP (sec)
Filling $[Z]$	140.5	34.4
Computation of $W_{2D}(\phi)$	1105.7	29.9

40 electric line sources for the fields inside of it. For the fields inside of the cylinder, the 40 line sources are assumed to radiate in a homogeneous medium of relative permittivity ϵ_r^c , and therefore these fields can be evaluated analytically. On the other hand, for the fields outside of the cylinder, the sources are assumed to radiate in the presence of the half-space, and therefore they are evaluated using the ND-SDP method. The continuity conditions were enforced on 80 testing points distributed uniformly on the boundary of the cylinder, leading to a 160×80 impedance matrix $[Z]$. The resulting matrix equation was solved in a least-squares sense and the 2-norm of the error in the continuity conditions, normalized to the incident field, was 0.004. After the amplitudes of the sources were calculated, the SI evaluation routine was used to obtain $W_{2D}(\phi)$ by computing the scattered electric field at 1000 points uniformly distributed on a circle of radius 10λ . The adaptive scheme described in Section VIII-A was used with a tolerance of 0.001. We also redid this computation with the older SI evaluation technique of [10], except that instead of using a trapezoidal rule with a fixed number of points as used there, we applied adaptive Gauss-Kronrod numerical integration with the same 0.001 tolerance. The computation times for both methods are shown in Table IV. A significant speed-up with respect to the method of [10] is evident, especially in the far-field calculation. Although it may seem natural use asymptotic methods for the far-fields, if the entire range of ϕ is of interest these methods usually require uniform asymptotic expansions and can become fairly complicated.

Two additional examples of the solution of scattering problems are shown Fig. 17. The electric field of the previous example, this time near the cylinder, is shown in Fig. 17(a). The continuity of the field across the media boundaries, which graphically appears perfect, attests to the validity of the solution. Lastly, as shown in Fig. 17(b), scattering from a groove in a dielectric half-space may be analyzed by modeling the groove as a half-buried cylinder with a permittivity equal to that of the $y > 0$ region. Like in the previous example, the continuity of the field appears to be perfect. In fact, a normalized error of 0.0055 in the continuity conditions resulted by using 60 basis functions. The total computation time for the 150^2 pixel image shown in Fig. 17(b) was about 8.5 minutes.

IX. SUMMARY

A numerical methodology for efficient evaluation of half-space SIs is described in this paper. The approach is based on a simple and efficient method for numerical determination of the SDPs, and is termed the ND-SDP method. The idea is to determine the path numerically by stepping in the direction of

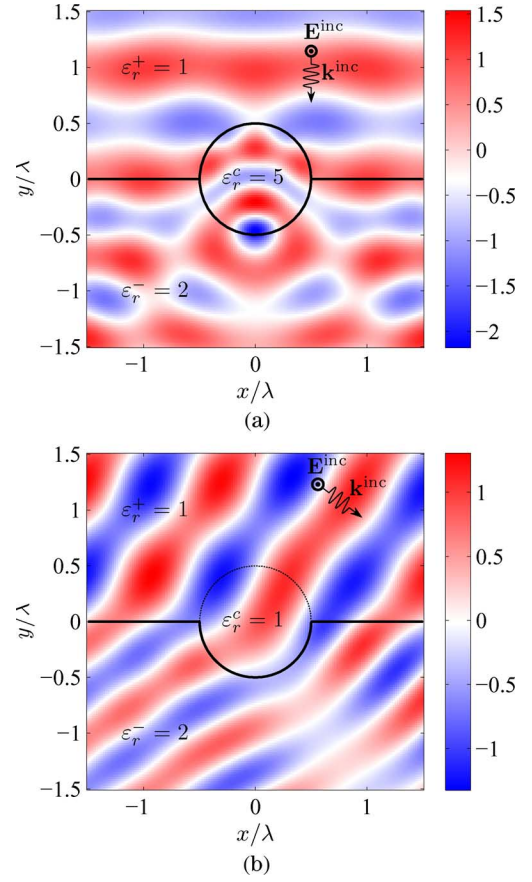


Fig. 17. The real part of the z -directed electric field near: (a) a half-buried dielectric cylinder, and (b) a semi-circular groove. In (a), all parameters are as in Fig. 16, whereas in (b), all parameters are also as in Fig. 16, except the incident wave vector, which is $\mathbf{k}^{\text{inc}} = k_0(0.8\mathbf{u}_x - 0.6\mathbf{u}_y)$, and the relative permittivity of the cylinder, which is $\epsilon_r^c = 1$.

steepest descent, starting at the saddle point. A fast method for accurate evaluation of the derivative of the path, necessary for the numerical integration, is also described. The time required for computation of the path and its derivative scales linearly with the number of integration points and is comparable to the time an analytical evaluation of these quantities requires, when such analytical expression exists. On the SDP, Gaussian quadrature can be used to obtain accurate results with just a few samples of the integrand. When a branch point is intercepted, a second path is added giving rise to a lateral wave contribution (in the reflected field case), or an evanescent wave contribution due to a second, complex, saddle-point (in the transmitted field case).

The numerical determination scheme is quite general and could be used to determine the SDPs of other spectral integrals. Other sources, such as dipoles and beams, and more general layered media configurations could be considered. In these cases, the path determination scheme would not have to be altered significantly, but the existence of other singularities would have to be taken into consideration.

A number of special cases, for which straightforward integration of SIs along the SDP yields poor results, were also considered. The special cases were: the critical angle case, the grazing angle case, and the quasi-static case. Alternative paths and specialized Gaussian quadrature rules were proposed for

these cases. The trade-off between accuracy and computational resources was investigated by testing the integration algorithms on a wide range of problem parameters. Also, the code was validated by comparison with published data and was shown to outperform the SI evaluation method of [10] by a significant margin. Lastly, some representative scattering problems, involving dielectric cylinders near a dielectric-half-space, were solved by use of the ND-SDP code.

ACKNOWLEDGMENT

Part of this work was performed while Y. Leviatan was a Visiting Professor at the University of Illinois at Urbana-Champaign. He would like to thank Provost L. Katehi and Prof. A. Cangellaris for their kind hospitality and for the valuable discussions he had with them.

REFERENCES

- [1] A. Sommerfeld, "Über die Ausbreitung der Wellen in der drahtlosen Telegraphie," *Ann. Phys.*, vol. 333, no. 4, pp. 665–736, 1909.
- [2] J. Zenneck, "Über die Fortpflanzung ebener elektromagnetischer Wellen längs einer ebenen Leiterfläche und ihre Beziehung zur drahtlosen Telegraphie," *Ann. Phys.*, vol. 328, no. 10, pp. 846–866, 1907.
- [3] L. Brekhovskikh, *Waves in Layered Media*. New York: Academic Press, 1960.
- [4] L. Felsen and N. Marcuvitz, *Radiation and Scattering of Waves*. Englewood Cliffs, NJ: Prentice-Hall, 1973.
- [5] W. C. Chew, *Waves and Fields in Inhomogeneous Media*. New York: Wiley, 1995.
- [6] Y. Rahmat-Samii, R. Mittra, and P. Parhami, "Evaluation of Sommerfeld integrals for lossy half-space problems," *Electromagnetics*, vol. 1, no. 1, pp. 1–28, 1981.
- [7] K. A. Michalski and J. R. Mosig, "Multilayered media Green's functions in integral equation formulations," *IEEE Trans. Antennas Propag.*, vol. 45, no. 3, pp. 508–519, 1997.
- [8] V. I. Okhmatovski and A. C. Cangellaris, "A new technique for the derivation of closed-form electromagnetic Green's functions for unbounded planar layered media," *IEEE Trans. Antennas Propag.*, vol. 50, no. 7, pp. 1005–1016, Jul. 2002.
- [9] K. A. Michalski and D. Zheng, "Electromagnetic scattering and radiation by surfaces of arbitrary shape in layered media, Part II: Implementation and results for contiguous half-spaces," *IEEE Trans. Antennas Propag.*, vol. 38, no. 3, pp. 345–352, 1990.
- [10] Y. Leviatan and Y. Meyouhas, "Analysis of electromagnetic scattering from buried cylinders using a multifilament current model," *Rad. Sci.*, vol. 25, pp. 1231–1244, 1990.
- [11] M. Paulus, P. Gay-Balmaz, and O. J. F. Martin, "Accurate and efficient computation of the Green's tensor for stratified media," *Phys. Rev. E*, vol. 62, no. 4, pp. 5797–5807, 2000.
- [12] Y. L. Chow, J. J. Yang, D. G. Fang, and G. E. Howard, "A closed-form spatial Green's function for the thick microstrip substrate," *IEEE Trans. Microw. Theory Tech.*, vol. 39, no. 3, pp. 588–592, 1991.
- [13] B. Wu and L. Tsang, "Fast computation of layered medium Green's functions of multilayers and lossy media using fast all-modes method and numerical modified steepest descent path method," *IEEE Trans. Microw. Theory Tech.*, vol. 56, no. 6, pp. 1446–1454, 2008.
- [14] F. J. Demuyneck, G. A. E. Vandenbosch, and A. R. Van de Capelle, "The expansion wave concept. I. Efficient calculation of spatial Green's functions in a stratified dielectric medium," *IEEE Trans. Antennas Propag.*, vol. 46, no. 3, pp. 397–406, 1998.
- [15] D. G. Fang, J. J. Yang, and G. Y. Delisle, "Discrete image theory for horizontal electric dipoles in a multilayered medium," *Proc. Inst. Elect. Eng.*, vol. 135, no. 5, pt. H, pp. 297–303, 1988.
- [16] J. Bernal, F. Mesa, and F. Medina, "2-D analysis of leakage in printed-circuit lines using discrete complex-images technique," *IEEE Trans. Microw. Theory Tech.*, vol. 50, no. 8, pp. 1895–1900, 2002.
- [17] E. A. Soliman and G. A. E. Vandenbosch, "Green's functions of filament sources embedded in stratified dielectric media," *Progr. Electromagn. Res.*, vol. 62, pp. 21–40, 2006.
- [18] I. Lindell and E. Alanen, "Exact image theory for the Sommerfeld half-space problem—Part I: Vertical magnetic dipole," *IEEE Trans. Antennas Propag.*, vol. 32, no. 2, pp. 126–133, 1984.
- [19] V. I. Okhmatovski and A. C. Cangellaris, "Evaluation of layered media Green's functions via rational function fitting," *IEEE Microwave Compon. Lett.*, vol. 14, no. 1, pp. 22–24, 2004.
- [20] K. A. Michalski, "On the efficient evaluation of integrals arising in the Sommerfeld halfspace problem," *Proc. Inst. Elect. Eng.*, vol. 132, pt. H, pp. 312–318, 1985.
- [21] M. Yuan and T. K. Sarkar, "Computation of the Sommerfeld integral tails using the matrix pencil method," *IEEE Trans. Antennas Propag.*, vol. 54, no. 4, pp. 1358–1362, 2006.
- [22] B. Hu and W. C. Chew, "Fast inhomogeneous plane wave algorithm for scattering from objects above the multilayered medium," *IEEE Trans. Geosci. Remote Sens.*, vol. 39, no. 5, pp. 1028–1038, 2001.
- [23] T. J. Cui and W. C. Chew, "Efficient evaluation of sommerfeld integrals for TM wave scattering by buried objects," *J. Electromag. Waves Appl.*, vol. 12, pp. 607–657, 1998.
- [24] T. J. Cui and W. C. Chew, "Fast evaluation of Sommerfeld integrals for EM scattering and radiation by three-dimensional buried objects," *IEEE Trans. Geosci. Remote Sens.*, vol. 37, no. 2, pp. 887–900, 1999.
- [25] K. A. Michalski, "Evaluation of Sommerfeld integrals arising in the ground stake antenna problem," *Proc. Inst. Elect. Eng.*, vol. 134, pt. H, pp. 93–97, 1987.
- [26] T. J. Cui, W. C. Chew, A. A. Aydinier, and Y. H. Zhang, "Fast-forward solvers for the low-frequency detection of buried dielectric objects," *IEEE Trans. Geosci. Remote Sens.*, vol. 41, no. 9, pp. 2026–2036, 2003.
- [27] G. Szegő, *Orthogonal Polynomials*, 3rd ed. Washington, DC: American Mathematical Society, 1967.
- [28] W. Gautschi, *Orthogonal Polynomials: Computation and Approximation*. Oxford, U.K.: Oxford University press, 2004.
- [29] [Online]. Available: <http://www.webee.technion.ac.il/people/leviatan/ndsdp/index.htm>
- [30] R. F. Harrington, *Time-Harmonic Electromagnetic Fields*. New York: McGraw-Hill, 1961.
- [31] H. L. Bertoni, L. B. Felsen, and J. W. Ra, "Evanescent fields produced by totally reflected beams," *IEEE Trans. Antennas Propag.*, vol. 21, no. 5, pp. 730–732, 1973.
- [32] P. J. Davis and P. Rabinowitz, *Methods of Numerical Integration*. New York: Wiley, 1975.
- [33] J. W. Ra, H. L. Bertoni, and L. B. Felsen, "Reflection and transmission of beams at a dielectric interface," *SIAM J. Appl. Math.*, vol. 24, no. 3, pp. 396–413, 1973.
- [34] A. Ishimaru, *Electromagnetic Wave Propagation, Radiation, and Scattering*. Englewood Cliffs, NJ: Prentice-Hall, 1991.
- [35] L. M. Brekhovskikh and O. A. Godin, *Acoustics of Layered Media II: Point Sources and Bounded Beams*. Germany: Springer-Verlag, 1990.
- [36] W. Gautschi, "Orthogonal polynomials (in Matlab)," *J. Comput. Appl. Math.*, vol. 178, no. 1–2, pp. 215–234, 2005.
- [37] D. K. Kahaner and G. Monegato, "Nonexistence of extended Gauss-Laguerre and Gauss-Hermite quadrature rules with positive weights," *ZAMP*, vol. 29, no. 6, pp. 983–986, 1978.
- [38] Y. Leviatan and A. Boag, "Analysis of electromagnetic scattering from dielectric cylinders using a multifilament current model," *IEEE Trans. Antennas Propag.*, vol. 35, no. 10, pp. 1119–1127, 1987.
- [39] Y. Leviatan, A. Boag, and A. Boag, "Generalized formulations for electromagnetic scattering from perfectly conducting and homogeneous material bodies-theory and numerical solution," *IEEE Trans. Antennas Propag.*, vol. 36, no. 12, pp. 1722–1734, Dec. 1988.
- [40] Y. Leviatan and A. Boag, "Analysis of TE scattering from dielectric cylinders using a multifilament magnetic current model," *IEEE Trans. Antennas Propag.*, vol. 36, no. 7, pp. 1026–1031, 1988.
- [41] D. I. Kaklamani and H. T. Anastassiou, "Aspects of the method of auxiliary sources (MAS) in computational electromagnetics," *IEEE Antennas Propag. Mag.*, vol. 44, no. 3, pp. 48–64, Jun. 2002.
- [42] A. Ludwig and Y. Leviatan, "Analysis of bandgap characteristics of two-dimensional periodic structures by using the source-model technique," *J. Opt. Soc. Am. A*, vol. 20, no. 8, pp. 1553–1562, Aug. 2003.
- [43] A. Hochman and Y. Leviatan, "Analysis of strictly bound modes in photonic crystal fibers by use of a source-model technique," *J. Opt. Soc. Am. A*, vol. 21, no. 6, pp. 1073–1081, June 2004.
- [44] A. Hochman and Y. Leviatan, "Efficient and spurious-free integral-equation-based optical waveguide mode solver," *Opt. Express*, vol. 15, pp. 14 431–14 453, 2007.
- [45] E. Marx, "Scattering by an arbitrary cylinder at a plane interface: Broadside incidence," *IEEE Trans. Antennas Propag.*, vol. 37, no. 5, pp. 619–628, 1989.



Amit Hochman (S'08–M'09) received the B.Sc., M.Sc., and Ph.D. degrees in electrical engineering in 1996, 2005, and 2009, respectively, all from the Technion-Israel Institute of Technology, Haifa.

He spent a large part of his army service (1997–2002) at RAFAEL, working on the simulation of adaptive antennas and communication systems. He is currently a Postdoctoral Fellow at the Massachusetts Institute of Technology, Cambridge, where he is a member of the Computational Prototyping Group at the Research Laboratory of Electronics.

His research interests center around the development of efficient computational modeling schemes, primarily for optical devices with wavelength-scale features.

Riesman Chair in Electrical Engineering. During his tenure at the Technion he held short-term visiting positions at Cornell University, the Swiss Federal Institute of Technology (ETH) in Zurich, the Catholic University of America, the University d'Aix-Marseilles III, the University of Washington, Bell Laboratories, the University of Michigan, Purdue University, and the University of Illinois Urbana-Champaign. During 1989–1991, while on sabbatical leave from the Technion, he was with the Department of Electrical Engineering and Computer Science at The George Washington University as a Distinguished Visiting Professor.

Professor Leviatan's research interests include computational methods applied to antennas, electromagnetic wave scattering, and microwave as well as optical guiding structures. He has published more than 100 journal papers and is listed among ISI's Highly Cited Researchers. He also presented numerous papers at international symposia. He is a recipient of the 2001 Henry Taub Prize for Excellence in Research. He is a member of Commission B of the International Union of Radio Science.



Yehuda Leviatan (S'81–M'82–SM'88–F'98) received the B.Sc. and M.Sc. degrees in electrical engineering from the Technion-Israel Institute of Technology, Haifa, in 1977 and 1979, respectively, and the Ph.D. degree in electrical engineering from Syracuse University, Syracuse, NY, in 1982.

He spent the 1982/83 academic year as an Assistant Professor at Syracuse University and subsequently joined the Department of Electrical Engineering at the Technion, where at present he is a Professor and the incumbent of the Joseph and Sadie